

COSMOLOGY WITH CONTAMINATED SAMPLES: METHODS OF MEASURING DARK ENERGY WITH PHOTOMETRICALLY CLASSIFIED PAN-STARRS SUPERNOVAE

DAVID O. JONES¹, D. M. SCOLNIC^{2,3}, A. G. RIESS^{1,4}, R. KESSLER³, A. REST⁴, R. P. KIRSHNER^{5,6}, E. BERGER⁵, C. A. ORTEGA¹, R. J. FOLEY⁷, R. CHORNOCK⁸, P. J. CHALLIS⁵, W. S. BURGETT⁹, K. C. CHAMBERS⁹, P. W. DRAPER¹⁰, H. FLEWELLING⁹, M. E. HUBER⁹, N. KAISER⁹, R.-P. KUDRITZKI⁹, N. METCALFE¹⁰, R. J. WAINSCOT⁹, C. WATERS⁹

Draft version November 17, 2016

ABSTRACT

The Pan-STARRS (PS1) Medium Deep Survey discovered over 5,000 likely supernovae (SNe) but obtained spectral classifications for just 10% of its SN candidates. We measured spectroscopic host galaxy redshifts for 3,073 of these likely SNe and estimate that $\sim 1,000$ are Type Ia SNe (SNeIa) with light-curve quality sufficient for a cosmological analysis. We use these data with simulations to determine the impact of core-collapse SN (CCSN) contamination on measurements of the dark energy equation of state parameter, w . Using the method of Bayesian Estimation Applied to Multiple Species (BEAMS), distances to SNeIa and the contaminating CCSN distribution are simultaneously determined as a function of redshift. We test light-curve based SN classification priors for BEAMS as well as a new classification method that relies upon host galaxy spectra and the association of SN type with host type. By testing several SN classification methods and CCSN parameterizations on 1,000-SN simulations, we conservatively estimate that CCSN contamination gives a systematic error on w (σ_w^{CC}) of 0.014, 30% of the statistical uncertainty. Our best method gives $\sigma_w^{CC} = 0.005$, just 11% of the statistical uncertainty, but could be affected by incomplete knowledge of the CCSN distribution. Our method determines the SALT2 color and shape coefficients, α and β , with $\sim 3\%$ bias. Real PS1 SNe without spectroscopic classifications give measurements of w that are within 0.5σ of measurements from the PS1 spectroscopic sample. Finally, the inferred abundance of bright CCSNe in our sample is greater than expected based on measured CCSN rates and luminosity functions.

1. INTRODUCTION

Since the discovery of cosmic acceleration (Riess et al. 1998; Perlmutter et al. 1999), measuring the properties of dark energy with Type Ia supernovae (SNeIa) has been predicated on the spectroscopic confirmation of SNIa candidates. However, as the size of individual SNIa samples surpasses 1,000 SNe, obtaining spectra for each Type Ia candidate is becoming prohibitively expensive. Only a small fraction of SNeIa from current and future surveys such as the Dark Energy Survey (DES) and the Large Synoptic Survey Telescope (LSST) will have spectroscopic classification. Without spectroscopic classification, core-collapse SN (CCSN) contamination can bias our estimates of cosmological parameters (Falck et al. 2010; Kunz, Bassett, & Hlozek 2007).

Without SN spectroscopy, the shape and color of a

photometric SN light curve can be used as a less precise way to determine the type. Campbell et al. (2013) used light curves to classify 752 SNe as likely Type Ia, enough to measure the dark energy equation of state, w , with $\sim 10\%$ statistical uncertainty. Their sample was selected from light curve properties and a classifier that compares each observed light curve to SNIa and CCSN templates (PSNID; Sako et al. 2011). Their final sample comprised just 3.9% CCSNe. While Campbell et al. (2013) is the *only* SNIa-based measurement of w to date that does not use spectroscopic classification for its SNe, the measurement does not include systematic uncertainties. In addition, contaminating CCSNe bias their measurements of SNIa dispersion and the correlation between SN luminosity and light curve rise/decline rate by $\sim 60\%$.

Many light curve classifiers use the “naïve Bayes” approximation, which assumes all observables that indicate SN type are uncorrelated. Machine learning techniques can often outperform these classifiers, yielding higher SNIa classification efficiency (the fraction of SNeIa classified correctly) and lower CCSN contamination (Lochner et al. 2016; Möller et al. 2016). On SDSS SN data, the Sako et al. (2014) kd-tree nearest neighbor (NN) method has a purity comparable to Campbell et al. (2013) but accurately classifies ~ 1.4 times as many real SNeIa.

An important caveat is that nearly all classifiers are optimized on simulations with little evaluation on real data. Simulations, in turn, depend on CCSN templates and knowledge of the CCSN luminosity functions (LFs) and rates. CCSNe are diverse, far more so than SNeIa, and only a limited number of high-quality templates are publicly available. Training a classifier directly on sur-

¹ Department of Physics and Astronomy, The Johns Hopkins University, Baltimore, MD 21218.

² University of Chicago, Kavli Institute for Cosmological Physics, Chicago, IL, USA.

³ Hubble, KICP Fellow

⁴ Space Telescope Science Institute, Baltimore, MD 21218.

⁵ Harvard-Smithsonian Center for Astrophysics, 60 Garden Street, Cambridge, MA 02138, USA

⁶ Department of Physics, Harvard University, Cambridge, MA 02138, USA

⁷ Department of Astronomy and Astrophysics, University of California, Santa Cruz, CA 92064, USA

⁸ Astrophysical Institute, Department of Physics and Astronomy, 251B Clippinger Lab, Ohio University, Athens, OH 45701, USA

⁹ Institute for Astronomy, University of Hawaii at Manoa, Honolulu, HI 96822, USA

¹⁰ Department of Physics, Durham University, South Road, Durham DH1 3LE, UK

vey data is possible but can be sub-optimal due to limited numbers of CCSNe observed and the dependence of classifier results on the specific survey characteristics (e.g. observing cadences, filters, and signal-to-noise ratios).

We can make SN classification less dependent on CCSN templates, LFs, and rates by incorporating host galaxy data. Because many SNe Ia have a $\gtrsim 1$ Gyr delay time between progenitor formation and explosion (Rodney et al. 2014), they are the only type of SNe found in early-type galaxies (with very few known exceptions; Suh et al. 2011). Foley & Mandel (2013) found that it was possible to accurately classify the $\sim 20\%$ of SNe Ia found in elliptical galaxies if the morphology of their host galaxy is known.

Though these results are encouraging, it is unlikely that light curve and host galaxy classification alone will enable a measurement of w as precise as measurements using spectroscopically classified SNe (e.g. Betoule et al. 2014, $w = -1.027 \pm 0.055$). A difference in w of 5% corresponds to a change of 0.02 mag from $z = 0$ to $z = 0.5$; if CCSNe are 1 mag fainter than SNe Ia on average, a bias of 0.02 mag can be induced by just 2% CCSN contamination at low- z in a survey like PS1. If the contaminating distribution of CCSNe is more than 1 mag fainter (this depends on survey Malmquist bias), it takes even fewer CCSNe to bias w by an equivalent amount.

A Bayesian method, however, could use the probabilities that SNe are of type Ia as priors to simultaneously determine distances to Ia and CCSNe without bias. We refer to this method as Bayesian Estimation Applied to Multiple Species (BEAMS) following Kunz, Bassett, & Hlozek (2007) (hereafter KBH07; see also Press 1997 and Rubin et al. 2015). KBH07 test BEAMS on a simplistic SN simulation and find that it gives near-optimal accuracy and uncertainties on SN Ia distances.

Hlozek et al. (2012) test BEAMS further with Monte Carlo simulations of the Sloan Digital Sky Survey SN survey (SDSS-SN; Frieman et al. 2008; Kessler et al. 2009a). BEAMS biases measurements of the cosmic matter and dark energy densities, Ω_M and Ω_Λ , by less than the statistical uncertainties in their simulations. Their results demonstrated that SDSS SNe without spectroscopic classification can significantly improve cosmological constraints relative to the SDSS spectroscopic sample (Kessler et al. 2009a). Hlozek et al. (2012) did not measure the systematic uncertainties from their method.

As with SDSS, Pan-STARRS (PS1) discovered far more SNe Ia than could be observed spectroscopically. Spectroscopically-confirmed SNe Ia from the first $\sim 1/3$ of PS1 have been used to measure cosmological parameters but constitute only a small fraction of the available data (Rest et al. 2014, hereafter R14; Scolnic et al. 2014b). In this study, we use PS1 SNe lacking spectroscopic classification (hereafter referred to as photometric SNe) as a tool for testing SN classifiers, understanding CCSN contaminants and measuring the systematic error due to CCSN contamination. In total, PS1 has 1,092 SNe with high quality light curves and spectroscopic redshifts that can be used to measure cosmological parameters (including a \sim few percent CCSN contamination). Here, we focus on the 969 likely SNe Ia with spectroscopic host galaxy redshifts, 143 of which are spectroscopically confirmed, in order to study a sample with fewer selection

biases (§2.1). The goal of this study is to develop the methods necessary to measure cosmological parameters robustly using PS1 photometric SNe. Our full cosmological results from these data will be presented in a future analysis.

In §2, we present the sample and our host galaxy redshift followup survey. §3 discusses our SNANA simulations of the PS1 sample and our assumptions about the CCSN population. §4 describes our Bayesian parameter estimation methodology. In §5 we test BEAMS on simulations and subsamples of PS1 photometric SNe. In §6 and §7 we test the robustness of these results by exploring several variants of the method. The uncertainties in our simulations and methodology are discussed in §8 and our conclusions are in §9.

2. THE PAN-STARRS PHOTOMETRIC SUPERNOVA SAMPLE

The Pan-STARRS medium deep survey covers 10 7-square degree fields in five broadband filters, with typical *grizP1* observational cadences of 6 images per 10 days and a 5 day gap during bright time during which *yP1* images are taken. Typical 5σ detection limits are ~ 23 AB mag for *grizP1*, albeit with significant variation. For a complete description of the PS1 survey, see Kaiser et al. (2010) and R14.

PS1 images are processed using an image subtraction pipeline that is described in detail in Rest et al. (2005) and R14. To measure final light curves for the PS1 photometric sample (and the full spectroscopic sample; Scolnic et al. in prep), we made several improvements to that pipeline. We more than doubled the typical number of images that are combined to create a deep template for subtraction and we improved our PSF star selection and zeropoint calibration. These improvements will be described in detail in Scolnic et al. (in prep.).

Pan-STARRS discovered 5,235 likely SNe during its four years of operation and obtained spectra for 520 SNe. We collected 3,073 spectroscopic host galaxy redshifts for these likely SNe (§2.1). In addition to SN candidates, we observed spectra for thousands of variable stars, AGN, flaring M dwarfs, and other transients that will be published in future work.

2.1. Host Galaxy Redshift Survey

During the PS1 survey, many SN host redshifts were measured using the Hectospec multi-fiber instrument on the MMT (Fabricant et al. 2005; Mink et al. 2007). Near the end of PS1 operations, we began an additional survey with Hectospec to obtain redshifts for as many unobserved hosts as possible. Redshifts were also obtained with the Apache Point Observatory 3.5m telescope¹¹ (APO), the WIYN telescope¹², and for the southernmost PS1 field, the Anglo-Australian Telescope (AAT). We chose candidate host galaxies for follow-up in a largely unbiased way; we did not prioritize SNe based on their magnitudes, colors, or whether or not a SN spectrum had previously been obtained. Approximately 500 of our redshifts come from SDSS (Smee et al. 2013) or

¹¹ <http://www.apo.nmsu.edu/arc35m/>

¹² The WIYN Observatory is a joint facility of the University of Wisconsin-Madison, Indiana University, the National Optical Astronomy Observatory and the University of Missouri.

Table 1
Redshift Follow-up Summary

Telescope	Instrument	SN Candidates ^a	$\lambda_{min} - \lambda_{max}$ Å	Avg. Exp. Time min.	Approx. Resolution Å pix ⁻¹	z_{median}
AAT	AAOmega	512	3700 – 8500	180	6	0.15
APO	DIS	10	3500 – 9800	60	2.5	0.24
MMT	Hectospec	2348	3700 – 9200	90	5	0.33
SDSS	BOSS	250	3800 – 9200	45	2.5	0.20
WIYN	Hydra	45	3700 – 6500	180	4.5	0.34
Other ^b	...	296	0.19
Total	...	3,073	0.30

Note. — Some transient hosts were observed with multiple telescopes. Numbers include host observations of both spectroscopically confirmed and unconfirmed SN candidates.

^a Number of SN candidates with reliable redshifts.

^b Includes redshifts from 2dFGRS (Colless et al. 2003), 6dFGS (Jones et al. 2009), DEEP2 (Newman et al. 2013), VIPERS (Garilli et al. 2014), VVDS (Le Fèvre et al. 2005), WiggleZ (Blake et al. 2008) and zCOSMOS (Lilly et al. 2007).

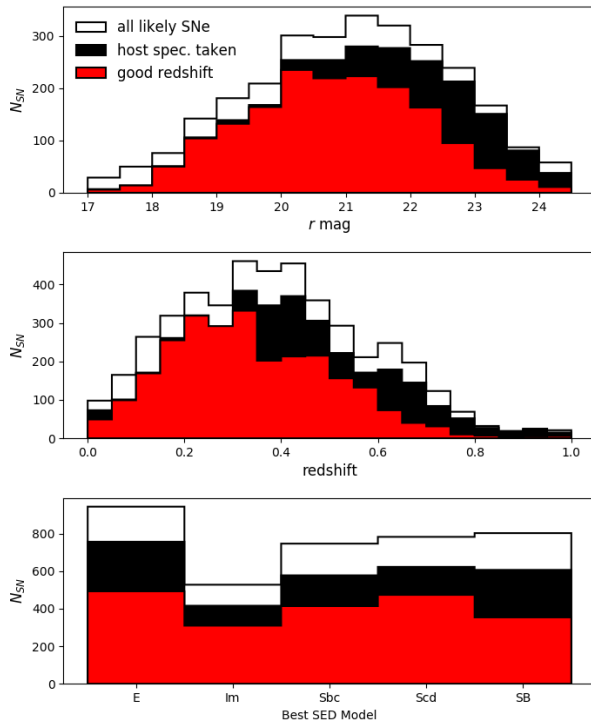


Figure 1. Host properties from PS1 as a function of r mag, redshift, and best-fit SED model. Out of the full sample of 5,235 PS1 SNe (white; host galaxy photo- z), we observed 3,930 hosts (black; photo- z) and measured accurate redshifts for 3,073 (red; spec- z). Our redshift survey has nearly 100% success to $r = 21$ and has a median redshift of 0.30. We obtained redshifts for a large number of both emission-line and absorption-line galaxies.

other public redshift surveys¹³.

We used the galaxy size- and orientation-weighted R parameter to identify the most likely host galaxy for each SN (Sullivan et al. 2006). The isophotal limit of a galaxy corresponds to $R \sim 3$. We use the redshift of the host galaxy with the lowest R if it has $R \leq 5$ following Sullivan et al. (2006). See Gupta et al. (2016) for a similar but more rigorous method of identifying SN host galaxies.

¹³ We include redshifts from 2dFGRS (Colless et al. 2003), 6dFGS (Jones et al. 2009), DEEP2 (Newman et al. 2013), VIPERS (Garilli et al. 2014), VVDS (Le Fèvre et al. 2005), WiggleZ (Blake et al. 2008) and zCOSMOS (Lilly et al. 2007).

To estimate the fraction of SNe for which we incorrectly determined which galaxy was the host, we compared redshifts derived from the spectroscopic redshifts of SNe to the spectroscopic redshifts of their most likely host galaxies. We found that only 2 of 169 hosts with reliable redshifts had evidence for a host galaxy mismatch, $|z_{SN} - z_{host}| > 0.02$. Both of these hosts had multiple large, nearby galaxies with $R < 5$. This mismatch fraction suggests that $1.2 \pm 0.5\%$ of our redshifts are incorrect due to mismatched hosts.

Compared to spectroscopically confirmed SNe, it is unlikely that photometric SNe have a significantly higher fraction of mismatched hosts. The spectroscopic targeting preferentially followed SNe with a larger separation from the center of their host galaxies or SNe with fainter hosts, as these SNe have spectra with less galaxy light contamination. The spectroscopically-confirmed sample has a median R of 2.5 while our photometric sample has a median R of 1.3.

The other source of incorrect redshifts is the measurement of velocities from host galaxy spectra. We measured redshifts by cross-correlating our spectra with galaxy templates (The RVSAO package; Kurtz & Mink 1998) and visually inspecting the results. Over the course of the survey, we observed over 1,500 transient hosts multiple times. For ~ 250 of these hosts, at least one observation yielded a redshift with a high Tonry & Davis (1979) cross-correlation parameter (TDR; $\gtrsim 9 - 10$).

By restricting our sample to hosts with $TDR > 4$ and redshifts of $0.01 < z < 0.75$, we measure a false redshift fraction of $1.4 \pm 1.3\%$. At $z > 0.75$, our simulations (§3) show that few SNe Ia or normal CCSNe could be discovered by PS1 or have their host redshifts measured with our program (Figure 1). Including mismatched hosts, the total percent of incorrect redshifts we expect is $2.6 \pm 1.4\%$. In §3 we simulate this fraction of false redshifts so that this effect will be incorporated in our BEAMS systematic error budget.

In total, we observed 3,863 host galaxies and have 3,073 reliable redshifts. The telescopes and instruments comprising our redshift survey are summarized in Table 1. Figure 1 shows the r magnitudes, redshifts, and best-fit SED model for the PS1 photometric sample. 87% of PS1 SNe with detectable host galaxies were observed with our redshift follow-up program and reliable redshifts

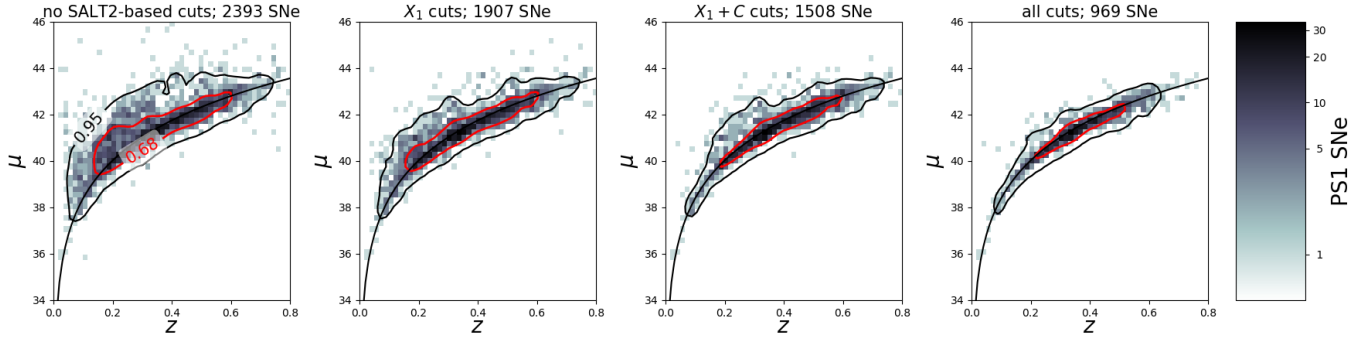


Figure 2. The effect of Betoule et al. (2014) cuts on the PS1 photometric Hubble diagram. Distance moduli are measured using the Tripp estimator (Eq. 1) with nuisance parameters from R14. Of the 2,393 SNe passing host separation and AGN cuts that are fit by SALT2, shape and color cuts remove 885, while χ^2 -based fit probability cuts and SNR-type cuts (shape uncertainty and time of maximum uncertainty) remove an additional 539 SNe, leaving 969. Each set of cuts removes a mix of SNe with poor light curve quality and CCSNe.

were measured for 73% of those galaxies. We measured redshifts for a large number of both emission-line and absorption-line galaxies. These data have a median redshift of 0.30.

2.2. SALT2 Selection

Throughout this work, we use the SALT2 model (Guy et al. 2010) to measure SN light curve parameters. We use those light curve parameters to standardize SNe Ia and select the SNe Ia that can best measure cosmological parameters. The Tripp estimator uses these SALT2 light curve parameters to infer the SN distance modulus, μ (Tripp 1998):

$$\mu_i = m_{B,i} + \alpha \times X_{1,i} - \beta \times C_i - M. \quad (1)$$

m_B is the log of the light curve amplitude, X_1 is the light curve stretch parameter, and C is the light curve color parameter. These parameters are all measured by the SALT2 fitting program, but deriving the distance modulus from them depends on the nuisance parameters α , β , and M . M is degenerate with the Hubble Constant, H_0 , and will be marginalized over during the cosmological parameter estimation.

To avoid unexpected biases in our sample selection, we use light curve selection requirements (cuts) from spectroscopically confirmed SN samples for the PS1 photometric SN sample. We make the same series of cuts to our SN light curves as Betoule et al. (2014) and add one additional cut on the SALT2 fit probability following R14. These cuts include uncertainty-based cuts that ensure the shape and time of maximum light of each SN is well-measured, and shape and color cuts that restrict our sample to SNe Ia for which the SALT2 model is well-trained. Our cuts are summarized in Table 2 and Figure 2. Out of 3,073 SNe with reliable host redshifts, SALT2 fits run successfully on 2,477 SNe (SALT2 parameter fitting often fails due lack of light curve data before or after maximum). 969 SNe pass all of our cuts.

Omitting the SALT2 σ_{X_1} cut has the largest single impact on our final sample. Without it, there would be over 1,300 SNe in the sample. The cut with the second largest reduction is the cut on C , without which there would be over 1,100 SNe (though many would be CCSNe). Although it may be possible to increase the SN sample size with relaxed cuts, the extent to which SNe Ia with low SNR and unusual colors are standardizable is not well

characterized.

In addition to the Betoule et al. (2014) cuts, we implement an additional set of cuts to remove possible AGN that were not flagged during the PS1 transient search. 86 SNe with both evidence of long-term variability and SN positions within $0.5''$ of their host centers were removed. After light curve cuts, removing likely AGN reduces our sample by just 18 SNe. We tuned our long-term variability criteria to find known AGN. We found that sources where $>25\%$ of background epochs have 2σ deviations from 0 are likely AGN (we define background epochs as <20 days before or >60 days after the discovery epoch). To avoid bias, we make these cuts (and all cuts) regardless of whether or not a given SN Ia is spectroscopically confirmed. The final Hubble diagram has 969 SNe with host redshifts after cuts.

2.3. Low- z SNe

Cosmological parameter constraints are greatly improved when a large, low- z SNIa sample is included to anchor the Hubble diagram. We use the same 197 low- z SNIa used in R14 though we anticipate adding additional low- z SNe in our full cosmological analysis. These SNe are spectroscopically confirmed and are assumed to have no CCSN contamination.

The R14 PS1 cosmology analysis has a low- z sample with higher intrinsic dispersion than the PS1 sample. The intrinsic dispersion, σ_{int} , is defined as the value added in quadrature to the SNIa distance modulus uncertainty such that the Hubble diagram reduced χ^2 is equal to 1 (Guy et al. 2007). Differences in SNIa intrinsic dispersion from survey to survey are typical, with the likely source of the variation including underestimated photometric difference image uncertainties and excess scatter from bright host galaxy subtractions (as seen in R14 and Kessler et al. 2015). Redshift evolution of the SNIa population could also play a role. We added 0.05 mag in quadrature to the m_B uncertainties of the low- z SNe to resolve the discrepancy. Once added, this additional uncertainty term gives both PS1 and low- z SNe the same intrinsic dispersion of ~ 0.115 mag.

3. SIMULATING THE PAN-STARRS SAMPLE

To robustly determine how CCSN contamination affects PS1 measurements of w , we require a simulation that encapsulates as many elements of the PS1 SN survey as possible. We used the SuperNova ANALYSIS soft-

Table 2
Sequential PS1 Data Cuts

	Removed	Remaining	This Cut Only	Without This Cut	Comments
Total candidates	...	5235
Host Sep $R < 5$	774	4461
Good host redshifts	1388	3073
Not fit by SALT2	596	2477
Possible AGN	84	2393	2393	987	...
$-3.0 < X_1 < 3.0$	486	1907	1964	1027	SALT2 light curve shape
$-0.3 < C < 0.3$	399	1508	1810	1125	SALT2 color
$\sigma_{\text{peakMJD}} < 2 \times (1+z)$	58	1450	2343	983	Uncertainty in time of max. light
$\sigma_{X_1} < 1$	370	1080	1690	1324	X_1 uncertainty
fit prob. ≥ 0.001	111	969	2040	1080	χ^2 and N_{dof} -based prob. from SALT2 fitter
$E(B-V)_{MW} > 0.15$	0	969	2477	969	Milky Way reddening

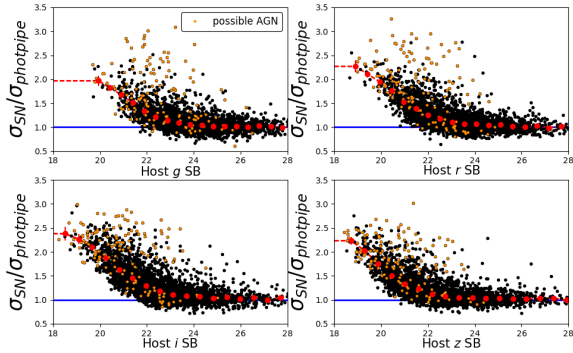


Figure 3. The ratio between “true” and DAOPHOT-derived photometric noise as a function of host galaxy surface brightness in the *griz*_{PS1} filters. We computed the host galaxy surface brightness by averaging over one PSF FWHM at the SN location. We computed the true photometric noise by inflating the errors from DAOPHOT (which do not include host galaxy noise) such that light curve epochs without SN light had $\chi^2 = 1$. Possible AGN (gold stars) comprise many of the outliers in this relation. We incorporated this relationship into our SNANA simulations to yield an accurate prediction of photometric uncertainties.

ware (SNANA; Kessler et al. 2009b) to generate Monte Carlo realizations of the PS1 survey. SNANA simulates a sample of SNe Ia and CCSNe using real observing conditions, host galaxy noise, selection effects, SN rates, and incorrect redshifts. Simulations assume a flat Λ CDM cosmology with $H_0 = 70 \text{ km s}^{-1} \text{ Mpc}^{-1}$, $\Omega_M = 0.3$ and $\Omega_\Lambda = 0.7$, and $w = -1$.

We choose not to simulate one significant effect: the correlation between SN luminosity and host mass (the host mass bias; Kelly et al. 2010; Lampeitl et al. 2010). We did not simulate the host mass bias because R14 did not include it (finding it had low significance in their sample), and we compare our PS1 photometric results directly to R14. This bias has been identified at $>5\sigma$ by Betoule et al. (2014) and we will include it in our future cosmological analysis with these data.

Each major component of our simulation is discussed in detail below:

1. Observing conditions. SNANA generates SN observations based on a simulation library file with observation dates, filters, sky noise, zeropoints, and PSF sizes that we measure from PS1 nightly images.
2. Host galaxies. The observed flux scatter of SNe

found in bright galaxies exceeds what is expected from Poisson noise alone (R14; Kessler et al. 2015). To correct for this, SNANA adds host galaxy noise to SN flux uncertainties by placing each SN in a simulated host galaxy. The SN is placed at a random location that has been weighted by the galaxy surface brightness profile. The distribution of PS1 host galaxies was determined from PS1 data; we measured the magnitudes and shape parameters of PS1 SN host galaxies using SExtractor, with zeropoints measured from the PS1 pipeline. We then use the noise model from Kessler et al. (2015):

$$\sigma_{flux} = \sigma_{flux} \times R_\sigma, \quad (2)$$

where R_σ is a function of host galaxy surface brightness (the vertical axis of Figure 3). We determined R_σ for PS1, comparing host surface brightness to the flux error scaling for which light curve epochs without SN flux have reduced $\chi^2 = 1$.

3. Selection effects. Two primary selection effects come into play in a photometric SNIa survey. The first is detection efficiency, the fraction of single-epoch detections as a function of the photometric SNR. The detection efficiency is computed by dividing the number of epochs detected by PS1 at a given SNR by the total number of epochs at that SNR. SNANA uses the efficiency vs. SNR, measured by PS1, to determine which simulated epochs are detected. SNANA then applies the PS1 survey requirement of three detections to “discover” a SN. The PS1 detection efficiency is $\sim 50\%$ for epochs with a SNR of 5 in the final light curves.

The second effect is host galaxy redshift selection. To model this effect, we incorporated a redshift-dependent “host galaxy efficiency” distribution in our simulations, which we adjusted such that the redshift distribution of the simulations matched our data.

4. Uncertainty adjustment. SNANA allows its simulated uncertainties to be scaled as a function of SNR such that the mean uncertainties in simulations match the mean uncertainties of our data. In PS1, this requires a modest $\sim 5 - 10\%$ noise increase at low SNR (after excess host galaxy noise is added). This adjustment is necessary due to the non-Gaussian wings of the PS1 PSF and the PSF fitting radius used by our pipeline.

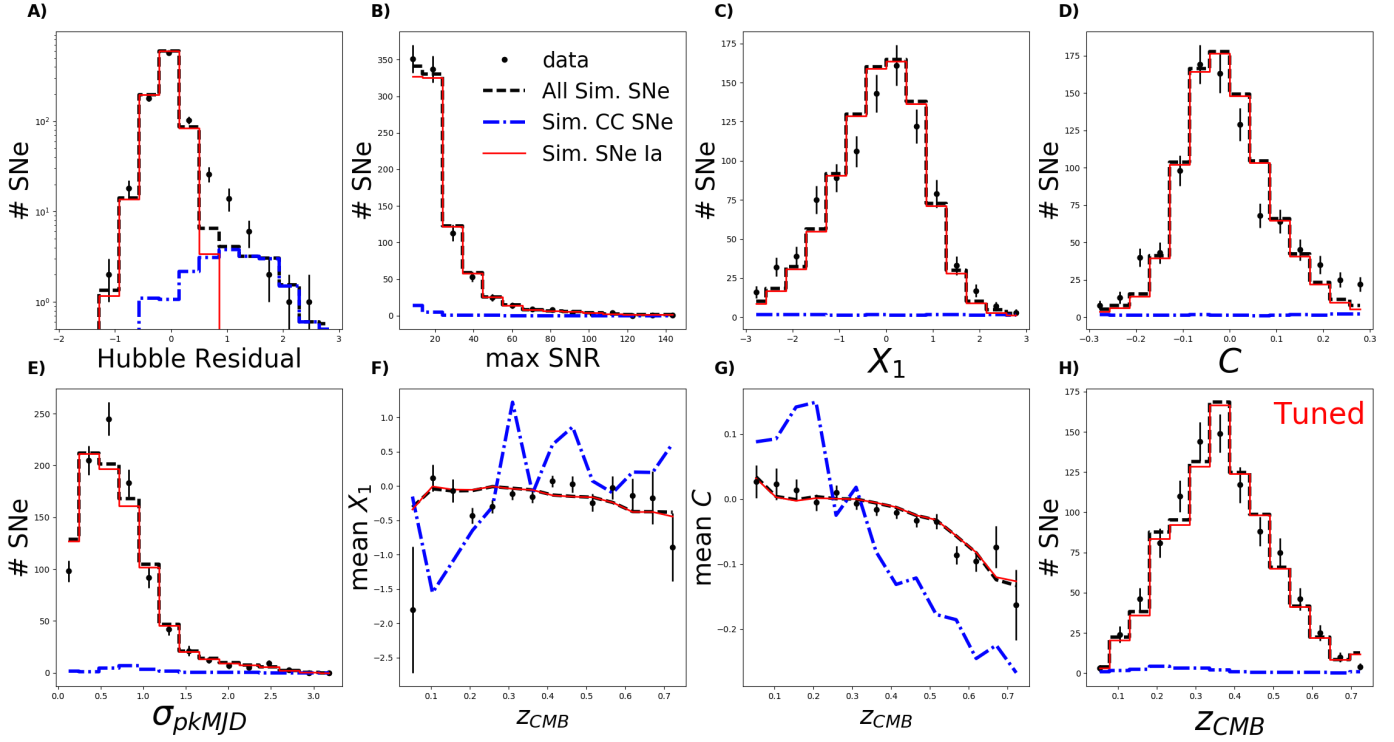


Figure 4. SNANA simulations of a PS1 photometric sample compared to PS1 data. The simulated Hubble residuals (A) of the CCSN distribution are flatter and fainter than the data. The simulated SNR (B), shapes (C), colors (D), uncertainties (E) and X_1/C redshift dependences (F and G) match our data closely, albeit with $\sim 3\sigma$ discrepancies in the time of maximum uncertainty and SN color. We tuned the simulated redshift distribution (H) to match our data.

5. Mismatched host galaxies and incorrect redshifts. As discussed previously, we expect $2.6 \pm 1.4\%$ of our redshifts to be incorrect due to mismatched host galaxies and redshift measurement uncertainties. We used SNANA to simulate incorrect host redshifts by assigning false, “measured” redshifts to 2.6% of our SNe. These redshifts are drawn from a flat, random distribution between $z = 0.01$ and $z = 0.75$. This is the range of redshifts at which PS1 can discover SNe, with the exception of rare superluminous SNe. Superluminous SNe typically have hosts too faint for our follow-up survey to measure their redshifts (Lunnan et al. 2015).

We find that $\sim 50\%$ of SNe with incorrect redshifts fail our sample cuts, giving a final contamination fraction of $\sim 1 - 1.5\%$. In large part, this reduction is due to cuts on the SALT2 color parameter. If a SN has an incorrect redshift, SALT2 is twice as likely to infer that its observed-frame colors are inconsistent with normal SNeIa when transformed to the wrong rest frame.

6. SNIa model. The SNIa model used in these simulations is the Guy et al. (2010) model with SNIa nuisance parameters from R14 (SALT2 $\alpha = 0.147$, $\beta = 3.13$). The simulated X_1 and C distributions were determined by Scolnic & Kessler (2016) for the PS1 spectroscopic sample. We adjusted the simulated means of the X_1 and C distributions by 1σ to better match our data, making X_1 lower and C higher. This difference is likely physical; on average, X_1 is lower and C is higher in massive host galaxies (e.g. Childress et al. 2013). Our host

follow-up program is most likely to obtain redshifts of massive galaxies.

7. CCSN templates and diversity. CCSNe are simulated based on a library of 43 templates in SNANA. The templates we use were originally created for the SN Photometric Classification Challenge (Kessler et al. 2010) and expanded by Bernstein et al. (2012, hereafter B12). Templates are based on bright, spectroscopically-confirmed SDSS, SuperNova Legacy Survey (SNLS; Conley et al. 2011; Sullivan et al. 2011), and Carnegie Supernova Project (Hamuy et al. 2006; Stritzinger et al. 2011) CCSNe with well-sampled light curves. Templates were created from the light curves by warping a well-sampled model spectrum for each SN subtype to match the light curve fluxes in every broadband filter (see §3.1.1).

SNANA has 24 II-P templates, 2 IIn templates, 1 II-L template, 7 Ib templates and 9 Ic templates. We added a subtype-specific magnitude offset to each template such that the mean simulated absolute magnitude of the subtype matched the mean of its Li et al. (2011) luminosity function (LF). By applying a uniform offset to every template in a subtype, the brightness of different templates relative to their subtype is incorporated in our simulations¹⁴. We also matched the dispersions of the Li et al. (2011) LFs by adding an additional, random

¹⁴ We tweaked this procedure for SNeIb, which had one anomalously bright template. All SNIb templates were adjusted by individual magnitude offsets such that each template matched the mean magnitude of SNeIb given by Li et al. (2011).

magnitude offset to each simulated CC SN. This offset was drawn from a Gaussian with a width we adjusted such that the dispersion of simulated absolute magnitudes for each subtype matched Li et al. (2011).

8. SN Rates. SNANA creates a combined SN Ia+CC simulation, with each SN type normalized by its rates. The redshift-dependent SN rates used in this work are the same as the baseline model of Rodney et al. (2014). SNe Ia follow measured rates, while CC SNe follow the cosmic star formation history. Relative rates of SN types and subtypes are anchored at $z = 0$ by Li et al. (2011) and evolve $\propto (1+z)^\gamma$, where γ is a free parameter tuned to match theory and observations (only a single value for γ is needed over the redshift range of PS1). We used $\gamma_{Ia} = 2.15$ and $\gamma_{CC} = 4.5$ (Rodney et al. 2014).

Figure 4 compares our simulations to the data after fitting all SNe with the SALT2 model. Note that CC SN information in this simulation is obtained without and PS1 analysis or input. SALT2 fitting is an effective way to examine both SNe Ia and the light curve parameters of Ia-like CC SNe. Figure 4 illustrates how the distribution of SN Ia light curve parameters and distances could be biased by misclassified CC SNe.

Our simulations agree closely with the data for most light curve parameters. The maximum SNR of simulated light curves matches the data (4B), as does the distribution of SALT2 X_1 (4C). However, there are too few simulated SNe with red SALT2 colors (4D) and there is a $\sim 2-3\sigma$ discrepancy in the distribution of time of maximum uncertainty (4E). The simulated redshift evolution of X_1 and C matches the data well (4F and 4G).

Though most simulated light curve parameters match our data well, the Hubble residuals (4A) do not. We see $\sim 2-3$ times more SNe than expected between $0.5 \lesssim \mu - \mu_{\Lambda\text{CDM}} < 1.5$ mag (these SNe are fainter than SNe Ia at their redshifts). This discrepancy is important to understand, as the properties of the CC SN distance distribution could affect how successfully the BEAMS method can measure CC SN and SN Ia distances.

3.1. Core-Collapse SNe

There are a few potential explanations for the difference in Hubble residuals between simulations and data. In this section, we attempt to identify the cause of the discrepancy.

First, a large percentage ($\gtrsim 20\%$) of inaccurate SN Ia redshifts could explain the data. However, in addition to disagreeing with our measurements, this would give too many simulated SNe with very bright and very faint Hubble residuals. Requiring a high TDR value and a small separation between the SN location and host galaxy center in our data does not resolve the conflict.

A second option is that the relative rates or magnitude distributions from Li et al. (2011) are erroneous or are biased by the targeted nature of the survey (LOSS searched for SNe in a set of pre-selected bright galaxies). These rates also do not take into account that the relative fractions of different CC SN subtypes could change with redshift. Modest adjustments, such as “tweaking”

the mean magnitudes or dispersions of CC SNe by $\lesssim 0.5$ mag, cannot explain the discrepancy. Simulating CC SNe using LFs from Richardson et al. (2014), which are typically $\sim 0.3-1.0$ mag brighter than Li et al. (2011), produces far too many bright CC SNe compared to our data. The effect of weak lensing on the data is expected to be an order of magnitude less than the size of the offset we see here (Smith et al. 2014).

By re-classifying LOSS SNe, Shivvers et al. (2016) recently found that SN Ib relative rates were more than double the fraction found by Li et al. (2011). This change could reduce the Hubble residual discrepancy by half or more. However, Shivvers et al. (2016) determined these rates by re-classifying a number of LOSS SNe Ic as SNe Ib, which in turn means that the SN Ib LF should be made fainter. Making the SN Ib LF fainter will increase the discrepancy in Hubble residuals. We continue to use Li et al. (2011) in this work, as we can be sure that the LFs and relative rates are self-consistent.

Finally, we consider that our results could be biased if SNANA templates have lower average reddening than PS1 data. In this work, we make the assumption that reddening in the templates is approximately equal to reddening in our data. This assumption allows us to use the Li et al. (2011) LFs, which have not been corrected for reddening, and SNANA templates, which also include intrinsic reddening. In reality, though PS1 tends to detect bright, unreddened CC SNe, there are likely substantial differences between the reddening distribution of the templates and the data. However, we find that adding additional reddening to our simulations tends to make the magnitude distribution of CC SNe more broad (we approximately adjust the Li et al. 2011 LFs for dust following Rodney et al. 2014). This *increases* the discrepancy between simulations and data. Correcting for the unknown intrinsic reddening of these templates is an important future objective that can allow SNANA simulations to be more realistic. See §8.1 for further discussion of biases in our simulations and templates.

3.1.1. Adding New Supernova Templates to SNANA

Several CC SN or peculiar Ia subtypes are missing from the SNANA simulation library but could be present in the PS1 data. Missing SN types include superluminous SNe, SNe I Ib, SNe Ibc-pec, and peculiar, faint SNe Ia such as 1991bg-like SNe Ia (Ia-91bg) and SNe Iax (Foley et al. 2013). Superluminous SNe are unlikely to help resolve the discrepancy, as they are brighter than SNe Ia and occur preferentially in faint hosts for which redshifts are difficult to measure (Lunnan et al. 2015). SNe Ibc-pec have similar LFs to SNe II-P but are much less common, so it is unlikely that many would fall on the Hubble diagram so near the SN Ia distribution. SNe Iax are red, fast-declining SNe that may be relatively common but have faint (albeit uncertain) LFs more similar to SNe II-P and Ibc-pec. These also tend to be poorly fit by SALT2, and would frequently fail our cuts.

SNe I Ib and SNe Ia-91bg both have LFs only ~ 1 mag fainter than SNe Ia, though they are relatively uncommon and would need a high fraction to pass SALT2 light curve cuts to be major contributors to our Hubble diagram. We investigated their impact by adding Ia-91bg and I Ib templates to SNANA.

To simulate CC SNe over a wide range of redshifts and

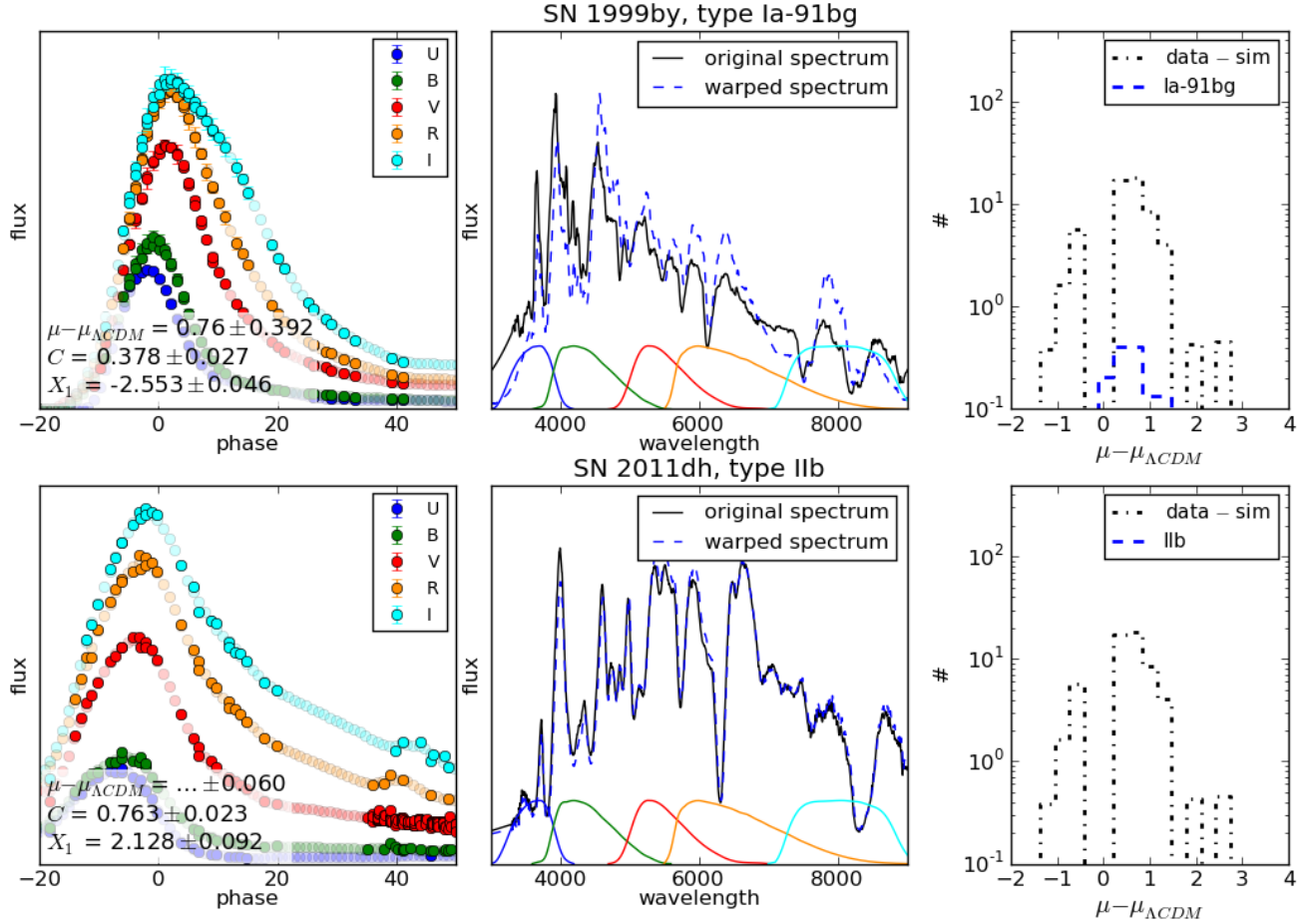


Figure 5. New templates for SNe Ia-91bg (top panels) and IIb (bottom panels) were added to SNANA by mangling a template spectrum to match light curve data. From left to right, we show the interpolated SN light curves (light shading indicates interpolated points), the warped template spectra at peak brightness, and the Hubble residuals of *all* the new subtype templates. We compare the Hubble residuals of the new templates to the difference between the data and our B12 simulations; the new templates cannot explain the discrepancy we observe between simulations and data. Because SN 2011dh has $z < 0.01$, its distance modulus residual is not shown in the left panel.

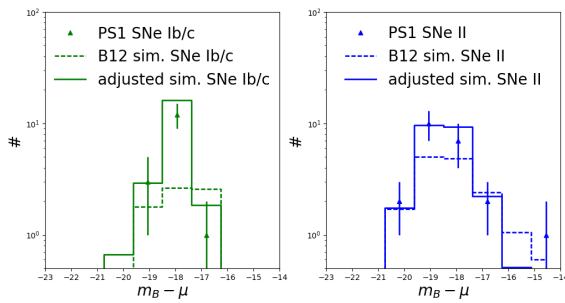


Figure 6. Empirical adjustments to SNANA simulations motivated by PSNID classifications, shown using histograms of SN absolute magnitude ($\text{SALT2 } m_B - \mu_{\text{ACDM}}$). PSNID-classified PS1 SNe and PSNID-classified simulations suggest that SNe Ib/c, after shape and color cuts, are brighter than expected. Our adjusted simulations (solid lines) match the data after we reduce the simulated Ib/c dispersion and brighten Ib/c LFs by ~ 1 mag.

passbands, SNANA templates require relatively high-SNR, high-cadence spectral and photometric sampling, which exists for a paucity of CC SNe. Simulating SN light curves at high redshift often necessitates near-ultraviolet data as well. To create a template, an interpolated, flux-calibrated spectral time series is “mangled” to match

the observed photometry by using wavelength-dependent splines with knots at the effective wavelengths of the photometric filters. Least-squares fitting determines the the best-fit spline that scales the spectrum to match the photometry. Hsiao et al. (2007) describes the “mangling” procedure in detail.

To improve the SNANA CCSN simulation, we add four SN IIb templates – SNe 1993J, 2008ax, 2008bo, and 2011dh – using spectra and light curves consolidated by the Open Supernova Catalog (Guillochon et al. 2016)¹⁵. Each of these templates have well-sampled spectra and optical light curves. We also add Ia-91bg templates using the SN 1991bg spectrum from Nugent et al. (2002)¹⁶, warped to match SNe Ia-91bg with well-sampled light curves before and after maximum (SNe 1991bg, 1998de,

¹⁵ References for the spectra and photometry are listed here. SN 1993J: Richmond et al. (1996); Metlova et al. (1995); Barbon et al. (1995); Jerkstrand et al. (2015); Modjaz et al. (2014). SN 2008ax: Modjaz et al. (2014); Brown et al. (2014); Taubenberger et al. (2011); Tsvetkov et al. (2009); Pastorello et al. (2008). SN 2008bo: Modjaz et al. (2014); Brown et al. (2014); Bianco et al. (2014). SN 2011dh: Ergon et al. (2015, 2014); Shivvers et al. (2013); Arcavi et al. (2011). Secondary sources: Yaron & Gal-Yam (2012); Richardson et al. (2001); Silverman et al. (2012) and the Sternberg Astronomical Institute Supernova Light Curve Catalogue.

¹⁶ https://c3.lbl.gov/nugent/nugent_templates.html

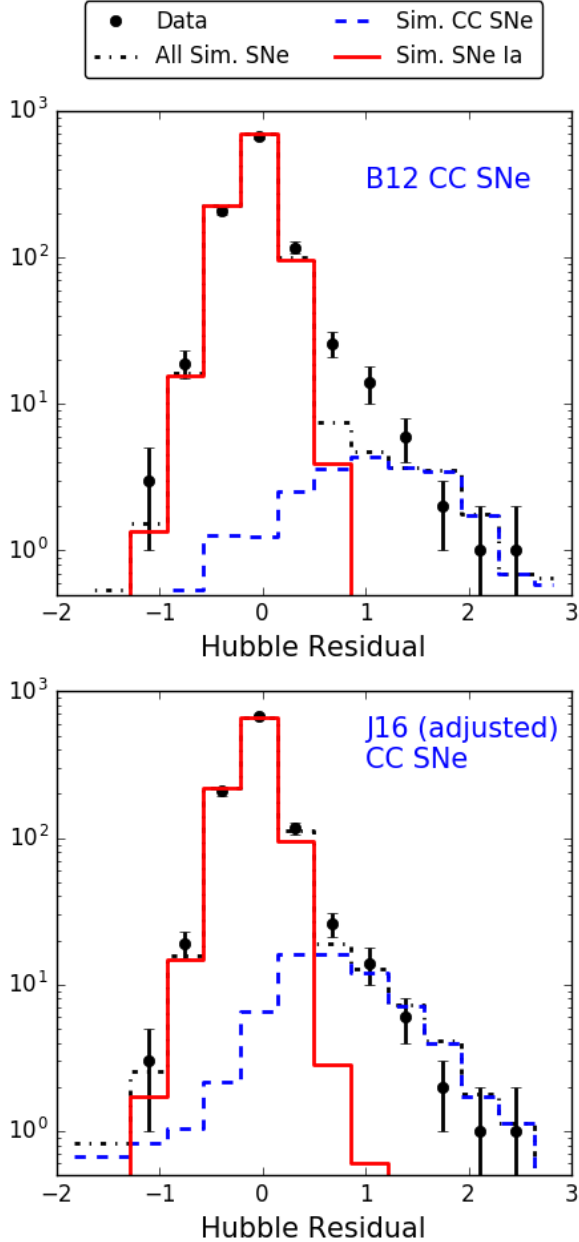


Figure 7. Comparison of Hubble residuals before and after empirical adjustments to CCSN LFs. We enlarge Figure 4A (top) and compare to our adjusted J16 simulations (bottom). Before empirical adjustments, the simulations contain just 2.4% CCSNe and are a poor match to the data. After adjustments, the simulations have 5.5% CCSNe. Discrepancies between data and simulations in the red end of the SALT2 C distribution and the time of maximum uncertainty distribution can both be explained by additional CCSNe.

1999by, 2005bl¹⁷). Using multiple SN templates helps us obtain better sampling of the shape-luminosity rela-

¹⁷ References for the photometry are listed here. SN 1998de: Silverman et al. (2012); Ganeshalingam et al. (2010); Modjaz et al. (2001). SN 1999by: Silverman et al. (2012); Ganeshalingam et al. (2010); Garnavich et al. (2004). SN 2005bl: Contreras et al. (2010). Secondary sources: the Sternberg Astronomical Institute Supernova Light Curve Catalogue.

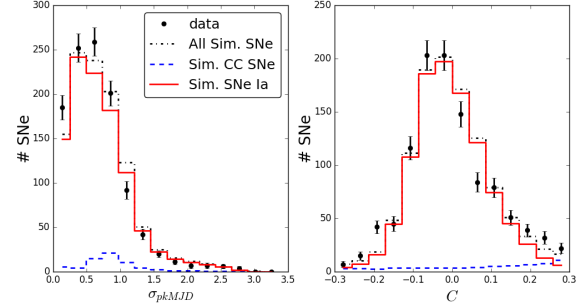


Figure 8. Simulated time of max. uncertainty (left) and SALT2 C (right), compared to data in the J16 simulations. Compared to the B12 simulations (Figure 4D and 4E), the time of max uncertainty and the red end of the C distribution are more consistent with our data in the J16 simulations.

tion for SNe 91bg (steeper than the relation for normal SNe Ia; Taubenberger et al. 2008).

Figure 5 shows the interpolated light curves, mangled spectra and Hubble residual histograms for SNe Iib and Ia-91bg. For Ia-91bg, we assume their rates have the same redshift dependence as SNe Ia. SNe Ia-91bg have magnitude distributions that could explain the data, but their rates are inconsistent with the data. SNe Iib are far too rare, as nearly all simulated SNe Iib have measured colors that are too red to be SNe Ia. Though we find that Ia-91bg and Iib SNe are not frequent enough to resolve the difference between PS1 data and simulations, we incorporate these subtypes in our simulations hereafter.

3.1.2. Measuring CCSN Luminosity Functions with PSNID

There is an additional procedure by which PS1 data can inform CCSN LFs: we use the PSNID light curve classifier (Sako et al. 2011, 2014) to separate the likely contributions of SNe Ia, Ib/c, and II. The SNANA implementation of PSNID compares the SALT2 SN Ia model and SNANA’s CCSN templates to the observed data. PSNID determines the fit χ^2 - and prior-based probability that a given SN is Type Ia, Type Ib/c, or Type II. Though the set of templates we use for PSNID is the same set we use to generate CCSNe in our simulations, broad priors allow these templates to be shifted in magnitude and extinction to fit our data.

We compare PSNID’s classifications of PS1 data and simulations by examining the distribution of $m_B - \mu_{\Lambda\text{CDM}}$, a proxy for absolute magnitude at peak (Figure 6). We find that likely SNe Ib/c are much brighter and have lower dispersion than the simulations. To bring our simulations into agreement with the data, we adjusted the simulated SN Ib/c and II distributions such that the mean and standard deviations of the *simulated* SNe that PSNID classified as Type Ib/c and II matched the mean and standard deviations of *real* PS1 SNe that PSNID classified as Type Ib/c and II. This requires reducing the dispersion of CCSN templates by 55% for SNe Ib/c and 30% for SNe II. It also requires brightening the simulated LFs by 1.2 mag for SNe Ib/c and 0.8 mag for SNe II. We made shape and color cuts (§2.2) in this analysis but neglected σ_{X_1} and σ_{peakMJD} cuts to increase our SN statistics.

Figure 6 shows the distributions of PSNID-classified PS1 SNe compared to our simulations before and after

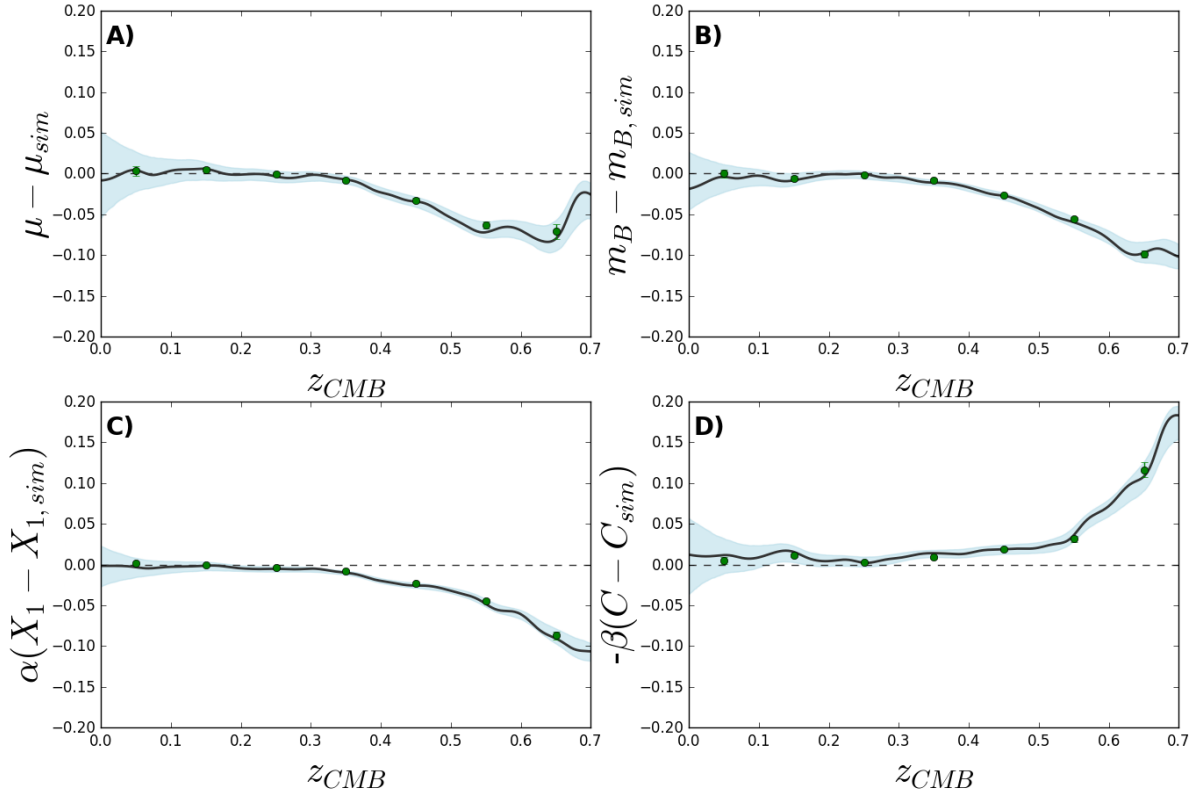


Figure 9. The redshift-dependent bias in distance (A), peak B magnitude (B), αX_1 (C), and $-\beta C$ (D) for the PS1 photometric sample using non-parametric spatial averaging (black lines with 95% confidence intervals in blue) with median bins (points) shown for comparison. The PS1 sample has negligible Malmquist bias until $z \sim 0.3$ and a maximum bias of ~ 0.1 mag at $z \gtrsim 0.6$.

absolute magnitude and dispersion adjustments. We apply shape and color cuts but neglect additional cuts to increase our CCSN sample size. Our simulations suggest a cut of $P(\text{SN Type}) > 99.99\%$ is necessary to limit the SNIa contamination in likely SNe Ib/c to $\lesssim 10\%$.

After these adjustments, simulated CC+Ia SNe are consistent with our data. Though likely SNe II in the data are consistent with simulations at the 1.2 σ level before adjustment, neglecting to adjust their magnitudes results in a $\sim 3\sigma$ discrepancy in the full data (even after SNIb/c magnitudes and dispersions are adjusted). Figure 7 shows Hubble residual histograms before and after our PSNID-based adjustments. After correction, CCSNe are 5.5% of our final sample and SNe Ia-91bg comprise 0.1%. The red tail of the SALT2 C distribution in Figure 4C can be explained by a simulation that detects additional CCSNe, as can the peak in time of maximum uncertainty at ~ 0.5 –1 days (Figure 8). No CCSN rate adjustments were made. Although the simulated absolute magnitudes have been brightened by ~ 1 mag, note that CCSN in the adjusted simulations are only ~ 0.5 mag brighter than the original simulation on average. This is because as we brighten the CCSN distribution, the number of detectable faint SNe – which are nearer to the peak of the LF, and thus occur more frequently – increases and reduces the mean absolute magnitude.

The CCSNe LFs in our adjusted simulation are $\sim 5\sigma$ brighter than Li et al. (2011). However, these results

do not necessarily imply that the true LFs of CCSNe show a $\sim 5\sigma$ inconsistency with Li et al. (2011). Rather, they indicate that our SALT2-based shape and color cuts isolate a region of CCSN parameter space that is not the average. Although we find it plausible that the CCSNe with shapes and colors most similar to SNe Ia have brighter and lower-dispersion LFs than CCSNe as a whole, further work is required to understand the diversity of CCSN sub-populations. Larger sets of high-cadence, high quality spectral time series from which to construct templates are also necessary. An additional factor is that the low statistics in the LOSS volume-limited sample require the shape of the CCSN LFs be extrapolated in some way. We treat CCSN LFs as Gaussian, most likely a flawed assumption (see Figure 16 of Li et al. 2011).

Our adjusted simulation matches the Hubble residuals of the PS1 data. It also resolves the discrepancies in the PS1 C and time of maximum uncertainty distributions (Figure 8). Hereafter, we refer to the simulation with a CCSN distribution derived from first principles as the B12 simulation and the adjusted simulation, which adds new CCSN templates and uses PSNID to infer the true SNIb/c distribution, as the J16 simulation¹⁸.

3.2. Malmquist Bias

¹⁸ Templates and simulation input files for this simulation have been added to the SNANA library.

We account for the SNIa Malmquist bias using PS1 and low- z simulations to determine the redshift-dependent bias of derived SNIa distances. We used Monte Carlo simulations of $\gtrsim 10,000$ SNe and non-parametric spatial averaging to determine and correct for the trend in distance modulus. Our spatial averaging algorithm uses local polynomial smoothing to interpolate the mean distance modulus trend across the redshift range.

Our simulations of the spectroscopically-confirmed low- z SN sample follow R14, who use the same α and β as our PS1 simulations. We found that our results reproduced the low- z sample accurately without adding host galaxy noise. The details of these low- z simulations and the determination of the spectroscopic selection function are discussed in detail in Scolnic et al. (2014a, see their Figure 6 for a comparison between simulations and data).

Figure 9 shows the simulated, redshift-dependent measurement bias in distance modulus, m_B , αX_1 , and $-\beta C$. The average high- z distance modulus bias in PS1 is nearly identical to the bias measured for PS1 spectroscopically-confirmed SNe by R14. One subtle difference is that the Malmquist bias is almost negligible in our sample until $z \sim 0.35$. Some differences in bias are expected because the R14 bias is dominated by their spectroscopic follow-up SN selection function.

At $z > 0.5$, we find the bias in X_1 , C , and μ becomes large as flux uncertainties near peak increase by up to a factor of 2. Greater than 50% of the m_B and C bias at these redshifts is due to our cut on X_1 uncertainty, which is effectively a SNR cut that favors bluer and brighter noise fluctuations. Distance biases in X_1 and C are also expected as the data become noisier and statistical fluctuations cause more SNe that fall outside the luminosity-correlated range to appear on our Hubble diagram (Scolnic & Kessler 2016, see their Figure 4). Our simulations also show that requiring lower X_1 uncertainty tends to select narrower measured light curve shapes. Accordingly, Figure 4E shows that the measured X_1 distribution remains largely flat with redshift; though SNe with larger X_1 values are intrinsically more luminous and thus more likely to be discovered, the measurement bias shown in Figure 9 has an opposite, and approximately equal, effect.

A discussion of systematic error in Malmquist bias determination will be presented in our future cosmological analysis. This will include incorporating α and β uncertainties, which can cause differences in the distance bias of ~ 5 mmag at $z > 0.5$. Although Scolnic et al. (2014a) found that the Malmquist bias is not one of the dominant sources of error, the photometric sample may be subject to different biases than a typical spectroscopic sample due to its lower average SNR.

4. COSMOLOGICAL PARAMETER ESTIMATION

We use the Bayesian Estimation Applied to Multiple Species (BEAMS) method to obtain SNIa distance measurements that are not biased by the CCSNe contaminating our data. BEAMS is presented in detail in KBH07. We briefly summarize the method below.

BEAMS simultaneously determines Ia and CCSN distances by sampling a posterior probability distribution that includes both SNIa and CCSN populations in the likelihood. The BEAMS posterior, the probability of the

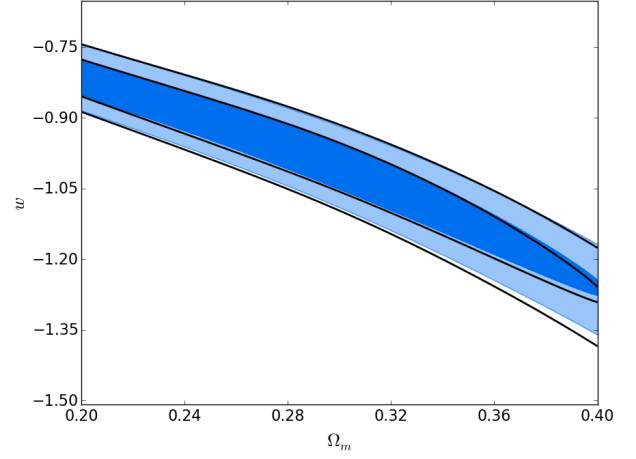


Figure 10. Comparing the full SNIa likelihood (filled contours) to the binned Ia likelihood (black).

free parameters θ given the data, D , is proportional to the product of the individual likelihoods for each SN multiplied by the priors on the free parameters:

$$P(\theta|D) \propto P(\theta) \times \prod_{i=1}^N \mathcal{L}_i. \quad (3)$$

The simplest suggested likelihood from KBH07 uses Gaussian distributions to represent CC SN and SNIa populations:

$$\begin{aligned} \mathcal{L}_i = & P_i(\text{Ia}) \times \frac{1}{\sqrt{2\pi(\sigma_{i,\text{Ia}}^2 + \sigma_{\text{Ia}}^2)}} \exp\left(-\frac{(\mu_{i,\text{Ia}} - \mu_{\text{Ia}}(z_i))^2}{2(\sigma_{i,\text{Ia}}^2 + \sigma_{\text{Ia}}^2)}\right) \\ & + P_i(\text{CC}) \times \frac{1}{\sqrt{2\pi(\sigma_{i,\text{CC}}^2 + \sigma_{\text{CC}}(z_i)^2)}} \exp\left(-\frac{(\mu_{i,\text{CC}} - \mu_{\text{CC}}(z_i))^2}{2(\sigma_{i,\text{CC}}^2 + \sigma_{\text{CC}}(z_i)^2)}\right). \end{aligned} \quad (4)$$

$P_i(\text{Ia})$ is the prior probability that the i th SN is of type Ia. $P_i(\text{CC})$, the probability that the SN is a CCSN, is equal to $1 - P_i(\text{Ia})$. $\mu_{i,\text{Ia}}$, $\mu_{i,\text{CC}}$ and $\sigma_{i,\text{Ia}}$, $\sigma_{i,\text{CC}}$ are the distance modulus and distance modulus uncertainties for the i th SN, derived using the Tripp estimator (Eq. 1). We differentiate between measured Ia and CC distance moduli from the data because we will allow the Tripp estimator to use different nuisance parameters for the SN Ia and CC SN terms in the likelihood (§4.1). μ_{Ia} , σ_{Ia} and μ_{CC} , σ_{CC} are the means and standard deviations of the SN Ia and CC SN Gaussians, respectively.

The variables μ_{Ia} and μ_{CC} are a function of the redshift, z , of the i th SN and of cosmological parameters. The variable σ_{CC} is redshift dependent as well, primarily due to the changing mix of CCSN subtypes that PS1 is able to discover as a function of redshift. We allow BEAMS to fit for these parameters by treating $\mu_{\text{Ia}}(z)$, $\mu_{\text{CC}}(z)$ and $\sigma_{\text{CC}}(z)$ as free parameters at certain fixed redshifts z_b . We refer to the set of fixed redshifts as “control points” following Betoule et al. (2014). Between two control points, the distance modulus (and dispersion) is interpolated by a linear function of $\log(z)$ defined by:

$$\begin{aligned} \mu(z) = & (1 - \xi)\mu_b + \xi\mu_{b+1} \\ \xi = & \log(z/z_b)/\log(z_{b+1}/z_b), \end{aligned} \quad (5)$$

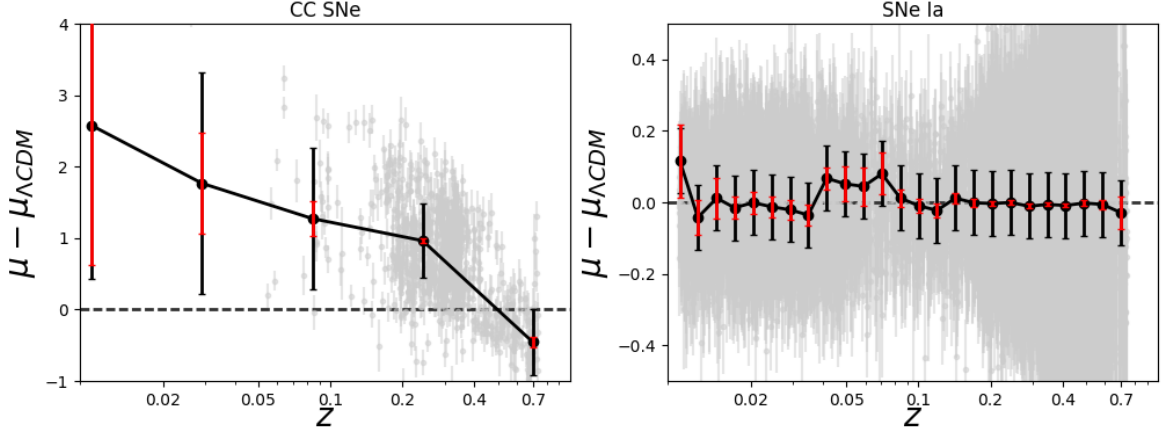


Figure 11. An illustration of BEAMS. Simulated CCSNe (left) and SNe Ia (right) with the redshift-dependent BEAMS parameters μ_{CC} , μ_{Ia} (black points) and σ_{CC} , σ_{Ia} (black bars). Uncertainties on μ_{CC} and μ_{Ia} are in red. We use correct prior probabilities of $P(Ia) = 1$ for all SNe Ia with correct redshifts and $P(Ia) = 0$ for all others.

where μ_b is the distance modulus at redshift z_b .

Betoule et al. (2014) fit to a set of 30 log-spaced redshift control points, and found that the difference between Λ CDM and the interpolation is always smaller than 1 mmag. We used 25 control points for the smaller PS1 redshift range of $0.01 < z < 0.7$ (we restrict our sample to $z < 0.7$, as very few PS1 SNe can be found at higher redshifts). In Figure 10, we compare the cosmological constraints from 1,000 individual SNe Ia to the approximate results derived from the SN Ia distances at 25 control points ($P(Ia) = 1$ for all SNe Ia). We find that the cosmological constraints are nearly identical.

We use 5 log-spaced redshift control points for CC SNe. If true SN type probabilities are known, 5 CC SN control points allows BEAMS enough flexibility to avoid biasing the Ia likelihood with a poor determination of the CC SN distribution. We allow the intrinsic width of the CC SN Gaussian distribution (σ_{CC}) to vary with redshift, but keep the intrinsic width of the SN Ia Gaussian fixed. This physically realistic assumption gives BEAMS more leverage to discriminate between SNe Ia and CC SNe, which have much higher dispersion than SNe Ia.

In total, our baseline implementation of BEAMS has 38 free parameters: 25 SN Ia distance moduli at Ia control points, 5 CC SN distance moduli at CC control points, 5 CC SN dispersion parameters, 1 SN Ia dispersion parameter, and the SALT2 nuisance parameters α and β which are used to compute μ_i and σ_i (discussed below). BEAMS free parameters can be efficiently estimated by sampling the logarithm of the posterior with a Markov Chain Monte Carlo (MCMC) algorithm. This work uses `emcee`¹⁹, a Python MCMC implementation (Foreman-Mackey et al. 2013). We use `emcee`'s Parallel-Tempered Ensemble Sampler to explore the multimodal peaks of the likelihood robustly. Figure 11 illustrates the Hubble residual diagram from BEAMS using simulated SNe and correct prior probabilities (all SNe Ia with correct redshifts have $P(Ia) = 1$ and all other SNe have $P(Ia) = 0$). Note that if few or no CC SNe are in a given redshift bin, the magnitude and uncertainty of CC SN distances are primarily determined by the priors.

We apply loose Gaussian priors on most BEAMS free

parameters, but find that with samples of 1,000 SNe or more, the difference between Gaussian and flat priors is negligible. For SN Ia distances, we apply flat priors. Though we assume some prior knowledge of the CC SN distribution, our priors on CC SN distance (μ_{CC} in Eq. 4) are very loose; we use broad Gaussians of width 3 mag that are centered at 2 mag fainter than SNe Ia at each control point. SALT2 nuisance parameters have Gaussian priors of width 5 times the uncertainties from R14. Our code is available online²⁰.

4.1. SALT2 Light Curve Parameters

We use a SALT2 fitting program to measure SN light curve parameters for our sample. However, SALT2 parameters do not directly measure the distance modulus (Eq. 1). For BEAMS to measure distances using SALT2 light curve fits, the nuisance parameters α and β must either be fixed to the value from a spectroscopic sample or incorporated into BEAMS as free parameters. We allow α and β to be free parameters here as it is a more general test of the method. Different survey methods, detection efficiencies, and selection criteria can significantly bias recovered SN parameters (Scolnic & Kessler 2016), which could make it necessary for future surveys to be able to fit for these parameters. In the CC SN component of the BEAMS likelihood, we fixed α and β to the nominal value for SN Ia spectroscopic samples for computational efficiency.

Because we include α and β as free parameters, the likelihood presented in Eq. 4 has a term in the Gaussian normalization factor, σ_i , that depends on α and β . The result is a significant bias in the derived SN parameters. This bias grows for larger SN samples (see Appendix B of Conley et al. 2011 and Kelly 2007 for details). The solution adopted in Conley et al. (2011) is to neglect the normalization term when determining α , β , and σ_{int} by using a simple likelihood $\mathcal{L} \propto \exp(-\chi^2/2)$. For 1,000 SNe, Conley et al. (2011) find that the bias from this likelihood is well below the statistical error (see Kessler & Scolnic 2016, §8.1). Though we cannot use this solution without biasing determinations of the CC SN and SN Ia distributions, we use an alternative formalism and

¹⁹ <http://dan.iel.fm/emcee/current/>

²⁰ <https://github.com/djones1040/BEAMS>

treat the uncertainties on the distance modulus as fixed in the denominator of the normalization term (independent of α and β). Fixing distance modulus uncertainties in the denominator does not bias α , β , or w and is a very modest approximation; in the PS1 sample, varying α and β within their 1σ errors from R14 gives a mean change in uncertainty of only 2 mmag. No individual SN has its uncertainty change by >20 mmag.

4.2. Prior Probabilities

The BEAMS formalism requires an estimate of the prior probability that a given SN is of Type Ia. This prior can be measured by a SN classifier, or it can be as simple as setting $P(\text{Ia}) = 1/2$ for all SNe. For our baseline analysis, we adopt the Nearest Neighbor method (NN) as applied in Sako et al. (2014). The NN classification probability uses a set of observables to define how close a given SN is to the CCSN and SNIa populations. In our implementation, we use the SALT2 color (C), stretch (X_1), and redshift (z). The equation:

$$d_i^2 = \frac{(z - z_i)^2}{\Delta z_{\max}^2} + \frac{(C - C_i)^2}{\Delta C_{\max}^2} + \frac{(X_1 - X_{1,i})^2}{\Delta X_{1,\max}^2} \quad (6)$$

defines a list of NN distances between the i th SN and simulated training data. For the i th SN, neighbors are defined as all simulated events with $d_i < 1$. NN training finds the parameters ΔC_{\max} , $\Delta X_{1,\max}$ and Δz_{\max} that optimize the classification metric (efficiency \times purity) of simulated training data. NN is an efficient and accurate classifier in PS1 simulations: the set of SNe with $P_{NN}(\text{Ia}) > 0.9$ has just 1.8% contamination compared to 7.0% contamination for the full sample (including CC SNe and SNeIa with incorrect redshifts). This set includes 64% of all SNeIa. See Kessler & Scolnic (2016) for details on the NN classification method.

We allow a re-mapping of the NN prior probabilities by adding two parameters to BEAMS: one that re-normalizes the probabilities, and a second that shifts them linearly. The first parameter is a scaling factor that corrects for globally skewed prior probabilities following Hlozek et al. (2012). This normalization term allows BEAMS to correct for effects such as incorrect redshift-dependent SN rates, inaccurate classifier training, or other $P(\text{Ia})$ biases. The second parameter is a global, linear shift in probability to handle incorrect typing near $P(\text{Ia}) = 0$ or $P(\text{Ia}) = 1$ (but requiring $0 < P(\text{Ia}) < 1$). This is necessary in cases where uncertainty in $P(\text{Ia}) \simeq 1$ or $P(\text{Ia}) \simeq 0$ is significant (KBH07). The relationship between the normalization factor, A , the shift parameter, S , and the probability $P(\text{Ia})$ is given by:

$$\tilde{P}(\text{Ia}) = \frac{A \times (P(\text{Ia}) + S)}{1 - (P(\text{Ia}) + S) + A \times (P(\text{Ia}) + S)} \quad (7)$$

$$0 < \tilde{P}(\text{Ia}) < 1.$$

Another solution suggested by KBH07 that could be explored in future work is adding a probability uncertainty term to the likelihood.

5. COSMOLOGICAL RESULTS FROM BEAMS

5.1. Tests with Simulated Data

We generated 25 simulations of 1,000 SNe each (25,000 total SNe) in order to test BEAMS on samples the size of the PS1 photometric sample. We include a simulated low- z sample of 250 SNe, the approximate number that will be included in our forthcoming cosmological analysis. The results presented here use the J16 simulations, as they have CC SN LF that match our data. Once distance moduli at the 25 redshift control points have been measured with BEAMS, those distances and distance covariance matrices can be used as inputs into the Cosmological Monte Carlo software for cosmological parameter fitting (CosmoMC; Lewis & Bridle 2002). We refer to BEAMS distance determinations in conjunction with CosmoMC fitting as the BEAMS method. For computational efficiency, we did not use the full Planck chains in this analysis and instead ran CosmoMC on our BEAMS results with a Planck-like prior of $\Omega_M = 0.30 \pm 0.02$.

To focus on biases from CC SN contamination, we define the CC SN bias Δ and the increase in statistical uncertainty due to CC SNe, $\Delta\sigma_{\text{stat}}$, for a given parameter P :

$$\Delta = P_m - P_{\text{Ia}}, \quad (8)$$

$$\Delta\sigma_{\text{stat}} = \sigma(P_m) - \sigma(P_{\text{Ia}}) \quad (9)$$

where P_m is the measured parameter from the BEAMS method and P_{Ia} is the measured parameter from the BEAMS method using SNeIa alone and setting all prior probabilities equal to one. For the 25 simulated samples, the average w_{Ia} value is -1.011 ± 0.008 . The RMS of w_{Ia} is 0.041, 88% of the mean statistical uncertainty (0.046).

We compare the Ia-only distances, SN parameters, and w measurements against our results from the BEAMS method in Table 3. Figure 12 shows that the binned distances are biased by less than 15% of their uncertainties with the exception of the final control point.

The SN parameters α and β are biased by 3%, or 1-1.5 times the average statistical error. σ_{Ia} is biased by 4%, -0.3 times the average statistical error. Note that σ_{Ia} (in Eq. 4) is functionally equivalent to the SN intrinsic dispersion, σ_{int} . These biases are small enough that they would be difficult to measure in real data. A possible cause of these biases is that Ia-like CC SNe have color laws more consistent with Milky Way dust ($\beta \sim 4.1$) and different shape-luminosity correlations.

We find w has a median bias of -0.0034 ± 0.0020 due to CC SN contamination, just 7% of the statistical error on w . The statistical uncertainty on w in this case is just 2% higher than the true statistical uncertainty. This result is consistent with KBH07, who find that BEAMS can yield nearly optimal uncertainties (we discuss BEAMS uncertainties further in §8.3).

If we compare the bias on w to a simpler method of measuring w with photometrically classified SNe, the advantage of using BEAMS is obvious. For our 25 1,000-SN samples, we make a simple cut of $P_{NN}(\text{Ia}) > 0.9$ and estimate cosmological parameters assuming that all SNe are Type Ia (Campbell et al. 2013 used a similar method of cutting the sample based on PSNID classifications). Making this cut removes 36% of true SNeIa in our sample and yields a final sample contaminated by just 1.8% CC SNe. In spite of this high sample purity, the average bias on w is -0.029, a factor of nine higher than our

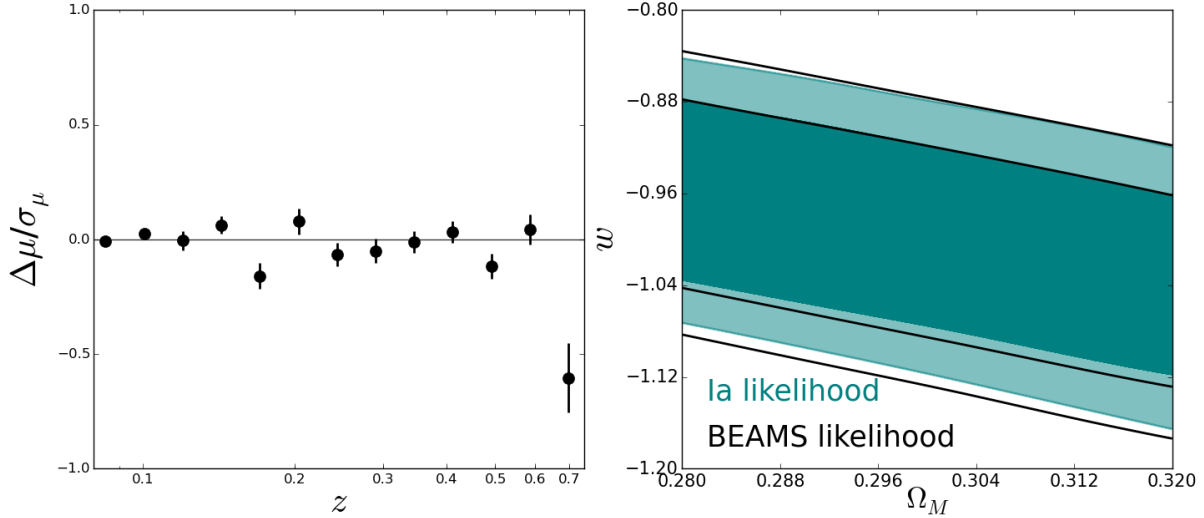


Figure 12. Left: Average distance modulus bias due to CCSN contamination (Eq. 11) as a fraction of the statistical uncertainty. Error bars are the uncertainty on the median bias from 25 samples. Right: 1σ cosmological parameter likelihood contours from BEAMS compared to the true likelihood using a representative sample of 1,000 SNe.

Table 3
Results from BEAMS

	Simulations			Data		
	bias	bias/ σ_{stat}	$\Delta\sigma_{stat}$	bias ^b	bias/ σ_{stat}	$\Delta\sigma_{stat}$
μ^a	-0.001 ± 0.001	-0.0	0.001 (1%)	-0.024 ± 0.022 (± 0.09)	-0.3	0.010 (11%)
α	0.005 ± 0.000	1.0	0.000 (1%)	-0.003 ± 0.000 (± 0.01)	-0.3	0.001 (14%)
β	0.094 ± 0.006	1.5	0.007 (11%)	0.067 ± 0.000 (± 0.12)	0.6	0.040 (33%)
w	-0.003 ± 0.002	-0.1	0.001 (2%)	-0.045 ± 0.016 (± 0.088)	-0.5	0.011 (12%)

Note. — Bias and increase in uncertainty due to CCSN contamination. All quantities shown are taken from the median of 25 samples. For simulations, bias is defined in Eq. 11. For data, the bias is defined as a given parameter measured using subsets of PS1 photometric SNe subtracted by that parameter measured using R14 SNe. We also show bias as a fraction of σ_{stat} , the statistical uncertainty on each parameter from a *single* sample.

^a Averaged over $0.08 < z < 0.7$.

^b Parameter uncertainties from R14 are in parentheses.

BEAMS results. Due to removing 36% of SNe Ia, the sta-
tistical uncertainty on w from this method is 10% higher,
compared to 2% higher from BEAMS. The dispersion of
the bias on w from sample to sample is also higher by a
factor of 3, meaning that the bias is more difficult to pre-
dict; 25% of our 25 samples returned a bias greater than
the statistical uncertainty on w . Without BEAMS, it is
unlikely that measuring cosmological parameters can be
competitive with spectroscopically-confirmed samples.

5.2. Comparing Real Pan-STARRS Photometric Supernovae to Rest et al. (2014)

Instead of analyzing the full PS1 sample, we analyze 25
random draws of PS1 SNe to compare R14 measurements
— and uncertainties — directly to measurements from
CCSN-contaminated samples of the same size. Because
96 R14 SNe Ia pass our sample cuts, we draw samples of
104 photometric SNe in order that our subsamples each
contain an average of 96 SNe Ia (and 8 CCSNe; we also
use reprocessed R14 light curves). We don't explicitly
require these random samples to have the same redshift
distribution as the PS1 spectroscopic sample. However,
the redshift distribution of the PS1 photometric sample

is similar to that of R14 (a nearly identical range and
median redshift).

For subsamples of PS1 data, we report parameter bi-
ases relative to R14:

$$\Delta = P_m - P_{R14} \quad (10)$$

$$\Delta\sigma_{stat} = \sigma(P_m) - \sigma(P_{R14}) \quad (11)$$

where P_{R14} and $\sigma(P_{R14})$ refer to a parameter and its
uncertainties from R14.

Although R14 does not have enough SNe to test for
small biases in w , the data still allow for a consistency
check that is independent of the myriad assumptions
made in simulations. In addition, the 96 SNe from R14
with low- z SNe can provide constraints on the bias of
nuisance parameters α , β , and σ_{Ia} due to the BEAMS
method. We include low- z SNe because BEAMS is more
robust when it has a spectroscopically-confirmed sample
as part of the data and has difficulty measuring accurate
dispersions for small samples.

We find that measured distances, SN nuisance param-
eters α and β , and w are consistent with R14 (Table

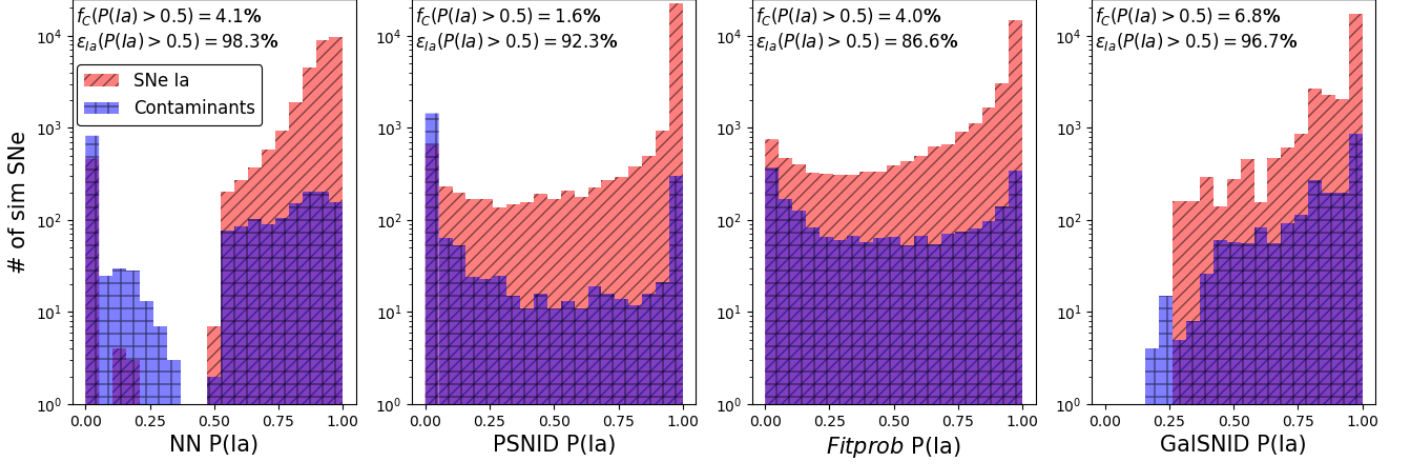


Figure 13. Simulated prior probabilities from the four classification methods discussed in this work for SNe Ia (red) and contaminants (blue; includes CC SNe and SNe Ia with incorrect redshifts). For each method, we show the percentage of contaminants f_C and the fraction of SNe Ia included, ϵ_{Ia} , in a $P(Ia) > 0.5$ sample. NN and PSNID separate CC SNe and SNe Ia effectively, with few SNe Ia but nearly all CC SNe having a low $P(Ia)$. *Fitprob* and GalSNID are much less precise, though the number of confirmed SNe Ia with low *Fitprob* is reduced after light curve cuts.

3). We could see the same hints of a bias toward higher values of β that we find in simulations but they are statistically insignificant. The bias in α is in the opposite direction of the bias we see in simulations but is not statistically significant (0.3σ).

The average of w from 25 104-SN samples is just 0.5σ lower than the measurements from reprocessed R14 light curves (σ is statistical uncertainty from R14). The uncertainties on w are 12% higher – and distance modulus uncertainties are 11% higher – likely due to the lower average SNR of photometric PS1 light curves.

6. EXPANDING THE BEAMS METHOD

The BEAMS method measures w with a marginally significant bias due to CC SNe of -0.0034 ± 0.0020 in simulations and a statistically insignificant bias in PS1 data. However, the reliability of these results could depend on the assumptions that we made when generating CC SN simulations and implementing BEAMS. We now expand our study of systematic uncertainties by applying alternative SN classification methods and adjusting the CC SN likelihood model. We discuss the methodology behind specific variants in this section and present all results from these variants in §7.

6.1. Additional $P(Ia)$ Priors

In addition to the NN prior probabilities in our baseline model, we use three additional methods of estimating $P(Ia)$: *Fitprob*, PSNID, and GalSNID. The effectiveness of each method is illustrated in Figure 13. The NN, *Fitprob*, and PSNID classifiers all determine probabilities by fitting to the photometric SN light curve. *Fitprob* relies on only the SALT2 model for fitting, while PSNID and NN depend on CC SN simulations for templates and training, respectively. GalSNID uses host galaxy information and depends on SNANA simulations only through the SN rates prior.

6.1.1. PSNID

The PSNID light curve fitter, as implemented in SNANA (Sako et al. 2011, 2014), fits observed SN light curves with perfect, noise-free simulations of the SALT2 SN Ia model and SNANA’s CC SN templates. PSNID estimates $P(Ia)$ from the χ^2 of the fit and includes type, redshift, and luminosity priors. PSNID is more accurate than the NN classifier by the metric in Figure 13, but PSNID has \sim twice as many contaminants with $P(Ia) > 0.95$, which could bias the BEAMS distances.

6.1.2. *Fitprob*

The *Fitprob* method estimates $P(Ia)$ from the χ^2 and number of degrees of freedom of the SALT2 light curve fit (the SALT2 fit probability). Because the SALT2 fit χ^2 has no knowledge about the relative frequency of different SN types, we multiplied $P_{fp}(Ia)$, the *Fitprob* probability, by a redshift-dependent SN rates prior, $P(Ia|z)$. $P(Ia|z)$ is the number of SNe Ia divided by the total number of SNe at a given redshift (after sample cuts; measured using the J16 simulations):

$$\tilde{P}_{fp}(Ia) = \frac{P(Ia|z)P_{fp}(Ia)}{P(CC|z)(1 - P_{fp}(Ia)) + P(Ia|z)P_{fp}(Ia)} \quad (12)$$

$$P(CC|z) = 1 - P(Ia|z).$$

Compared to the NN (baseline) classifier, *Fitprob* has a comparable fraction of contaminants at $P(Ia) > 0.5$. However, the fraction of CC SNe with high $P(Ia)$ is higher by a factor of $\sim 40\%$.

6.1.3. GalSNID

SNe Ia have much longer average delay times between progenitor formation and explosion than CC SNe. Because of this, SNe Ia are the only SN type found in early type hosts. This allows methods such as GalSNID (Foley & Mandel 2013) to classify SNe with host galaxy information. The GalSNID method in Foley & Mandel (2013) is based on photometric information and is highly dependent on host morphology. Because measuring galaxy

morphologies at typical PS1 redshifts requires $\sim 0.1''$ image resolution, we modified the method by adding spectral observables. Though GalSNID is a very inefficient classifier, it measures SN Ia probabilities in a way that is only minimally subject to light curve and LF uncertainties.

To train GalSNID, we used 602 host galaxy spectra from the Lick Observatory Supernova Search (LOSS; Leaman et al. 2011) and 354 host galaxy spectra of PS1 spectroscopically-confirmed SNe. The equivalent widths of spectral emission lines, and $H\alpha$ in particular, correlate with SN type. Another useful diagnostic is the template that cross-correlates best with the observed host spectrum. Finally, we include host galaxy R (labeled effective offset in Foley & Mandel 2013), $B - K$ colors and absolute K magnitudes from Foley & Mandel (2013). Our full methodology is presented in the Appendix, along with the Bayesian probabilities that a SN is of type Ia for different spectral parameters from our training sample. We use the naïve Bayes assumption for this work following Foley & Mandel (2013), which treats all observables as uncorrelated. In future work we hope to use machine learning techniques to improve GalSNID classifications.

To create GalSNID probabilities for the simulated sample, we artificially redshifted LOSS host galaxy spectra, added noise to make them consistent with the SNR of PS1 host spectra, and used GalSNID to measure the probability that each host observed a SN Ia. We took the distributions of GalSNID probabilities for the redshifted, noisy spectra corresponding to LOSS SNe II, Ib/c and Ia hosts in each simulated redshift bin and assigned the probabilities drawn from those distributions to simulated SNe II, Ib/c and Ia. This gave our simulated SNe the same probability distributions as the redshifted LOSS data. Figure 13 shows that GalSNID is a relatively imprecise classifier, but it provides constraints that are independent of SN light curves and their associated uncertainties. We have not taken into account the redshift evolution of SN host galaxies in this work.

On PS1 data, GalSNID is by far the least efficient classifier. Because classifications are highly influenced by the rates prior, GalSNID considers just 10% of contaminants to be likely CCSNe. If we set a higher threshold of $P(\text{Ia}) > 0.9$, GalSNID removes $\sim 30\%$ of CCSNe and keeps $\sim 70\%$ of SNe Ia. GalSNID is also most effective at $z \lesssim 0.35$, where $H\alpha$ is present in our optical spectra (the best indicator of SN type). Unfortunately for PS1, the largest SN Ia distance biases are at $z > 0.4$, where the CCSN distribution becomes blended with the SN Ia distribution.

GalSNID would also be useful as an additional prior on SN type in conjunction with other methods. However, due to uncertainty in CCSN models and LFs, in the present analysis we consider it most powerful as a standalone tool that can measure SN Ia probabilities without using light curve data.

6.2. Varying the CCSN Model

PS1 and other spectroscopic data show that SNe Ia are well-represented by a Gaussian Hubble residual model, but CCSNe are not. We investigated replacing the CCSN likelihood in Eq. 4 with two likelihoods that are more consistent with our CCSN simulations. We tested a two-Gaussian model with ten additional free parameters

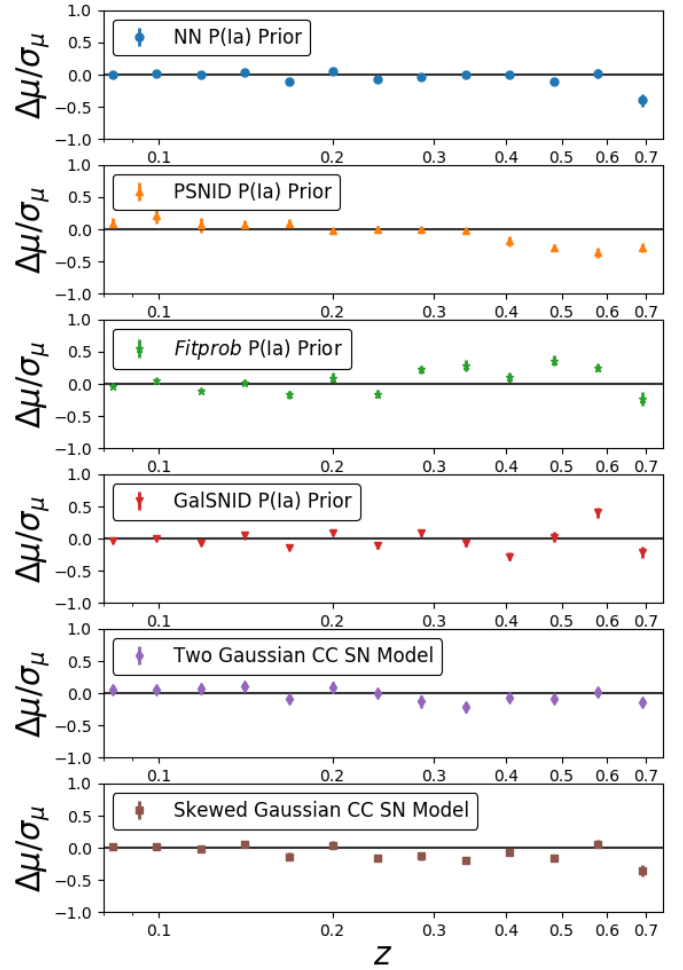


Figure 14. Distance bias due to CCSN contamination as a fraction of the distance uncertainty for each of our variants. Small systematic discrepancies begin to appear at $z > 0.4$. For PSNID, one control point is below the range of the plot: at $z = 0.7$, the distance is biased by an average of -1.5 times the statistical error.

ters for CCSNe (the means and standard deviations of the second Gaussian at five redshift control points). We also tested a single, asymmetric Gaussian model with five additional free parameters (skewness at each CCSN control point).

If we allow BEAMS to shift and/or rescale the prior probabilities that a SN is of type Ia (Eq. 7), BEAMS can give unphysical results. The alternative CCSN models are significantly more flexible and that flexibility must be constrained by accurate, fixed prior probabilities such as those from NN (see §8.3). We fix the parameters that allow BEAMS to adjust the priors (to $A = 1$ and $S = 0$ in Eq. 7) or else the uncertainties on SN Ia distances will inflate to > 0.1 mag for even our best-measured redshift control points.

7. RESULTS FROM BEAMS VARIANTS

In total, we test three additional methods of determining prior probability (PSNID, *Fitprob*, GalSNID) and two additional CCSN models. We test each variant on 25 samples of 1,000 simulated PS1 SNe and 25 samples of 104 real PS1 SNe. Though we discuss the ways in which distances and nuisance parameters are affected by these variants, we focus primarily on measurements of

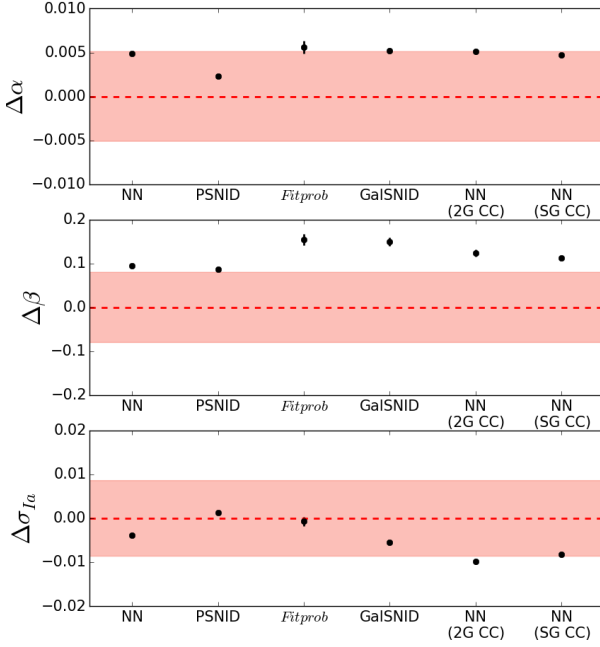


Figure 15. The bias in SALT2 α , β , and σ_{Ia} measured from 25 simulations of 1,000 SNe each, with shaded regions indicating typical uncertainties on each parameter from SN Ia-only samples. σ_{Ia} is too low by $\sim 0.005 - 0.01$, while α and β are too high by ~ 0.005 and ~ 0.1 , respectively ($\sim 1\sigma$). It is likely that reddened CC SNe are responsible for the higher color term (more consistent with Milky Way dust than the SN Ia color law). “2G CC” and “SG CC” refer to the 2-Gaussian and skewed Gaussian CCSN parameterizations, respectively

w . The RMS of these variants gives a conservative estimate of the systematic uncertainty on w , σ_w^{CC} , an error which could be reduced in the future by improved SN classification methods. It could also be reduced by testing our best single classifier on a robust set of CC+Ia SN simulations that include a larger set of CCSN templates and several methods of adjusting CCSN rates and LFs to match the data.

7.1. Simulations

σ_w^{CC} has an average value of 0.018 ± 0.009 (39% of the statistical error). The high uncertainty is due to the high dispersion of the systematic uncertainty from sample to sample. BEAMS distances (Figure 14) and nuisance parameters (Figure 15) are remarkably consistent, regardless of the method.

Table 4 and Figure 16 show the median bias and increase in uncertainty on w due to each P(Ia) method and CCSN model. *Fitprob* yields the most biased measurements of w , up to half the statistical uncertainty, while prior probabilities from PSNID and GalSNID bias w by ~ 0.01 . Using the two Gaussian CCSN model gives the smallest bias on w , though it increases the statistical uncertainty by 8%. Uncertainties on w are similar across all methods (see §8.3)

We compare these measurements of w to the case where BEAMS has minimal prior information: we set $P(Ia) = 1/2$ for all photometric SNe while still fixing $P(Ia) = 1$ for low- z SNe. The bias on w from this approach is -

Table 4
Cosmological Results from BEAMS Variants

Method	Δw	$\Delta w / \sigma_w$	$\Delta \sigma_w$
one Gaussian ^a	-0.003 ± 0.002	-0.1	0.001 (2%)
two Gaussians ^a	0.000 ± 0.006	0.0	0.004 (8%)
skewed Gaussian ^a	-0.005 ± 0.003	-0.1	0.001 (2%)
P(Ia) Method ^b			
	Δw	$\Delta w / \sigma_{w,Ia}$	$\Delta \sigma_w$
NN	-0.003 ± 0.002	-0.1	0.001 (2%)
PSNID	0.010 ± 0.005	0.2	0.002 (3%)
SALT2 Fit Prob.	-0.021 ± 0.004	-0.5	0.003 (5%)
GalSNID	-0.013 ± 0.004	-0.3	0.003 (5%)

Note. — Bias of w in simulations from each CCSN model and prior probability method. We take the median of 25 samples of 1,000 SNe. $\Delta w / \sigma_w$ is the median bias as a fraction of the statistical uncertainty on w . For each increase in uncertainty ($\Delta \sigma_w$), we show its percent increase in parentheses. Methods with the lowest bias and increase in uncertainty are highlighted in bold.

^a Using NN for the P(Ia) prior probabilities.

^b Using a single Gaussian CCSN model.

0.018, 40% higher than the GalSNID bias and is slightly lower than the *Fitprob* bias. However, the $P(Ia) = 1/2$ results have greater dispersion: the RMS of the bias on w for 25 samples is 17% greater than GalSNID and 40% greater than *Fitprob*.

If α and β are fixed to the values measured from spectroscopic samples, our method requires *surprisingly little prior information* to determine SN Ia distances robustly. Though fixing α and β does not improve NN and PSNID measurements of w , it allows the BEAMS method with *Fitprob* or GalSNID priors to measure w with a bias of just 0.006. This bias is nearly equivalent to that of our baseline method (NN priors and α and β as free parameters). If we fix α and β to the values measured from spectroscopic samples for *Fitprob* and GalSNID, σ_w^{CC} is reduced to 0.014, 30% of the statistical uncertainty.

For comparison, setting $P(Ia) = 1/2$ for PS1 SNe and fixing α and β gives results that have negligible average bias but also have high RMS. The mean bias on w is consistent with zero but has an RMS of 0.013, 44% higher than the RMS when using NN priors.

7.2. Pan-STARRS Data

Using 25 random samples of 104 PS1 photometric SNe, we see no evidence of bias on w and $\ll 1\sigma$ differences due to different prior methods and CCSN models. σ_w^{CC} is an average of 0.024, 27% of the statistical error. In Figure 18 we show that the *average* measurements of w from each variant have a lower dispersion of 0.011, just 13% the R14 statistical error.

Biases in nuisance parameters are similar to our baseline method (Figure 17). Just as we see in simulations, it appears that *Fitprob* and GalSNID appear to bias β more than other methods, though the difference has just $\sim 1\sigma$ significance. α and σ_{Ia} are largely consistent across all methods. It is likely that nuisance parameters in the real data appear less biased than in simulations because in PS1 data, the low- z spectroscopically confirmed sample is a much larger fraction of the full sample.

Figure 18 also shows the statistical uncertainties on w

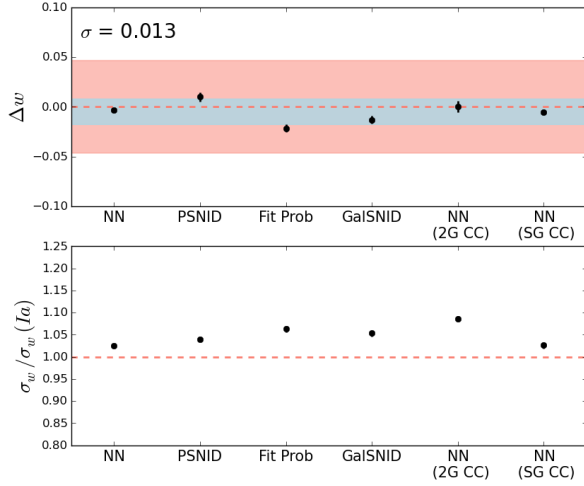


Figure 16. The w bias (top) and increased uncertainties (bottom) due to different $P(\text{Ia})$ priors and CCSN parameterizations in BEAMS. We show the median from 25 samples of 1,000 simulated SNe. In the top panel, the statistical error on w from SNe Ia is shown in red with the dispersion of different methods in blue. “2G CC” and “SG CC” refer to the 2-Gaussian and skewed Gaussian CCSN parameterizations, respectively.

from subsets of PS1 data. Uncertainties are higher than R14 by $>12\%$. The highest uncertainties come from *Fitprob* and *GalSNID*, which have up to 18% higher uncertainty on w than R14. Much of the increase in uncertainty in other variants is likely because PS1 photometric SNe have lower mean SNR than PS1 spectroscopically-confirmed SNe. R14 SNe have a median SNR at peak of ~ 50 , while photometric SNe have a median SNR at peak of just 16.

8. DISCUSSION

The PS1 photometric SN sample is the largest SNe Ia sample, but using it to optimally measure cosmological parameters requires accurate SN type probabilities. These in turn rely on our understanding of the PS1 sample and the CCSNe in it. Evaluating how our incomplete knowledge of CCSNe could bias the results is difficult. In this section, we discuss how CCSN simulations could be improved in the future. We also present alternatives to our implementation of BEAMS and measure the degree to which different methods and priors affect the statistical uncertainty on w .

8.1. Generating Reliable CCSN Simulations

Measuring the reliability of our method would be subject to fewer uncertainties if CCSN simulations were more robust. These simulations are currently subject to two primary limiting factors: the Gaussian assumption for the CCSN LF based on measured mean and RMS LFs and the imprecise measurement of the shape of CCSN LFs and the lack of CCSN template diversity.

Figure 19 shows that the assumption of the shape of CCSN LFs could have a strong impact on the fraction of bright CCSNe. While the Malmquist bias for SNe Ia is ~ 0.1 mag at maximum, CCSNe observed at the median PS1 survey redshift are up to 3 magnitudes – and 2-3 standard deviations – brighter than the peak of their LF. Determining the frequency of such bright CCSNe

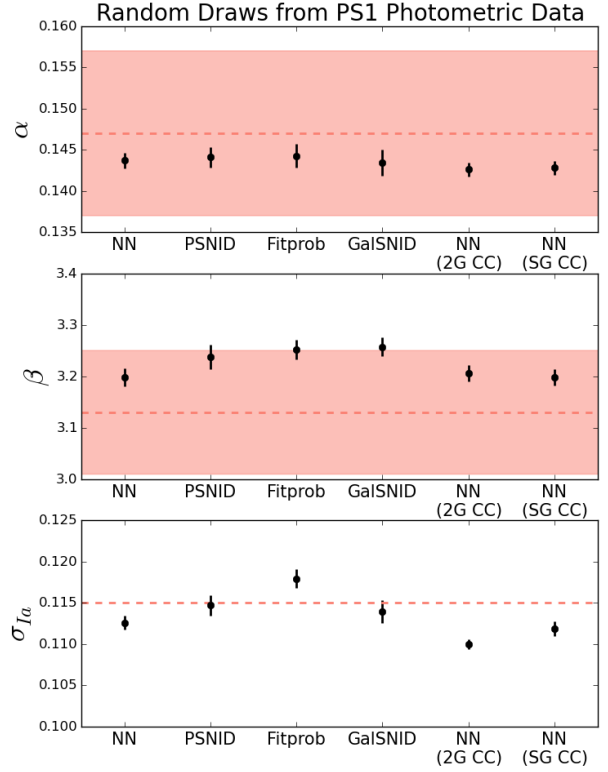


Figure 17. Nuisance parameters from 25 Monte Carlo samples of PS1 photometric data, including a low- z sample, compared to values from R14 (dashed lines) and their uncertainties (shaded regions). Values from all methods are consistent with each other and with the spectroscopic sample, though we see possible $0.5\text{--}1\sigma$ hints of the bias in β that we see in simulations. “2G CC” and “SG CC” refer to the 2-Gaussian and skewed Gaussian CCSN parameterizations.

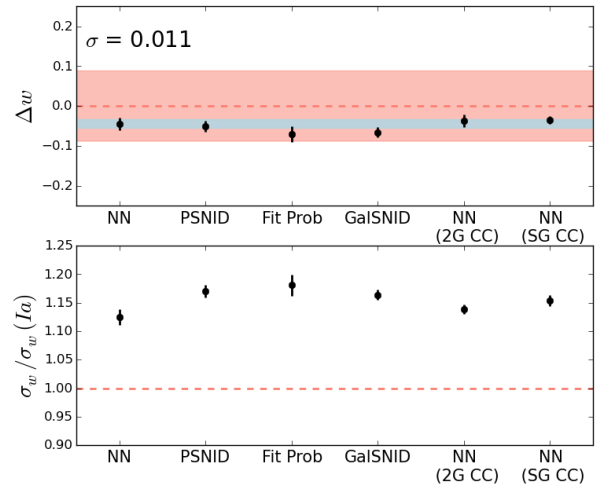


Figure 18. Figure 16, but with random draws from real PS1 data compared to R14. Measurements of w are consistent with R14 at the $\sim 0.5\sigma$ level (they are lower by -0.045 for NN). The highest uncertainties come from the *Fitprob* and *GalSNID* methods.

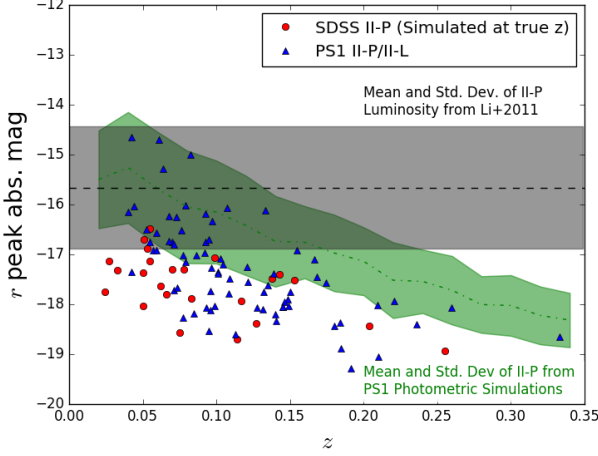


Figure 19. Spectroscopically confirmed Type II SNe from PS1 (blue triangles; Sanders et al. 2015) and SDSS (red circles) compared to simulations of the PS1 photometric sample (green). The SDSS SNe shown here were used to create the SNANA templates used in this study. They are typically 2-3 σ brighter than the mean magnitude of the population from Li et al. (2011, gray). These SDSS templates are made fainter to match the gray bar and then simulated to yield the green contours.

requires measuring the shapes of their LFs with better statistics than what is currently available from volume-limited surveys such as Li et al. (2011). Due to low statistics, our current simulations treat the LFs of each SN subtype as Gaussian, a flawed assumption.

Generating more robust simulations also requires additional, diverse CC SN templates. Our simulations sample the luminosity, shape, and color distribution of most CC SN subtypes with just a few templates. In addition, the luminosity distribution of these templates is heavily biased; nearly all CC SNe currently used as templates are much brighter than the mean luminosity of their subtypes. Our method makes these bright templates fainter to match the Li et al. (2011) LFs, implicitly assuming that faint CC SNe have similar light curves to bright CC SNe. A better approach would be to have CC SN templates that sample the full range of luminosity space for CC SNe.

We note that additional high-SNR CC SN light curves and spectra exist, but require careful smoothing, interpolation, and spectral mangling to be a reliable addition to the SNANA template library. We have added SNe Ia-91bg and SNI Ib templates to SNANA, but assembling and mangling all available CC SN light curves and templates is beyond the scope of this work.

In the absence of additional templates and improved LF measurements, we can use GalSNID and *Fitprob* classifications to give measurements of w some degree of independence from these sources of uncertainty. Though these classifiers are suboptimal compared to classifiers such as NN, they give a unique set of probabilities that do not rely on simulations for training (though *Fitprob* is implicitly dependent on the nature of CC SN light curves contaminating our sample). *Fitprob* and GalSNID *explicitly* depend on simulations only through their rates priors. Adjusting these priors by a factor of 2 biases w by $\sim 20\%$ of the statistical uncertainty or less.

8.2. Alternatives in Implementing BEAMS

In determining cosmological parameters with the BEAMS method we made a set of choices that minimized the number of free parameters while still reproducing the full cosmological parameter likelihoods. We found that most choices made little difference, provided that we had a large number of MCMC steps and few enough parameters. Though future improvements could include adding additional CC SN bins at high redshift, we don't find that this changes our results significantly.

Two additional choices can improve the systematic error due to CC SN contamination. First, though fixing α and β does not improve the accuracy of the BEAMS method when using NN or PSNID priors, it does improve the accuracy when using *Fitprob* and GalSNID, methods with less accurate classifications. With α and β fixed, *Fitprob* and GalSNID are *no more biased* than the more sophisticated light curve based methods. If we choose to either keep α and β fixed in all BEAMS variants or just in the *Fitprob* and GalSNID variants, we find that the σ_w^{CC} decreases by $\sim 25\%$ on average. In Pan-STARRS, spectroscopically-confirmed SNe can measure these parameters with low uncertainty, and fixing them for our future cosmology analysis in some or all methods could be advantageous.

The second method of improving BEAMS is by cutting additional likely CC SNe from the sample. Following Kessler & Scolnic (2016), we tested a cut on the NN prior probability by requiring $0.5 < P_{NN}(Ia) < 1$. Our simulations show that this cut removes $\sim 50\%$ of CC SNe but just 2% of SNe Ia. The rejected sample has $\sim 50\%$ CC SN contamination. Because our baseline BEAMS analysis uses NN probabilities, an NN probability cut yields no improvements to our baseline results. However, when this cut is added to our other classification methods, it reduces σ_w^{CC} by $\sim 30\%$ on average. We have not included this cut in our systematic error analysis (§7) as it makes our classification methods more correlated and adds an additional dependence on uncertain simulations to the measured systematic error. However, it is likely that this cut will increase the consistency of the full PS1 cosmological results.

A third option for BEAMS is to estimate SNIa distances with a more strict CC SN model. Kessler & Scolnic (2016) adopt an approach where BEAMS CC SN distributions are determined directly from simulations. For our PS1 analysis, we have adopted a more general approach to CC SNe at the cost of several additional parameters to marginalize over and a simpler form of the likelihood (Kessler & Scolnic 2016 also suggest adding free CC SN parameters as a possible improvement to their method). Our tests show our parameterization is capable of marginalizing over the simulated CC SNe such that the Ia likelihood is recovered, and our method is slightly more general than a simulation-based method. A simulation-based mapping of CC SNe may be more robust, but validating it thoroughly is beyond the scope of this paper. In particular, the influence of inaccurate simulations on its recovered results must be explored fully.

8.3. Uncertainties in BEAMS Distances

By setting $P(Ia) = 1/2$ for all photometric SNe, the BEAMS method measures w with a bias of -0.019, 0.4

times the statistical uncertainty on w . The statistical uncertainty on w , even with no prior information as to which SNe are of Type Ia, is just 5% higher than using SNe Ia alone. This is primarily due to two factors: the loose priors we employ and the fact that we include a sample of low- z spectroscopically-confirmed SNe Ia for which $P(\text{Ia})$ is fixed to 1. These low- z SNe Ia help set the SN Ia dispersion and the SN parameters α and β , which are fixed as a function of redshift.

If we remove the low- z sample, distance and SN parameter biases increase. Distance uncertainties, which are higher by just $\sim 10\%$ when using the $P(\text{Ia}) = 1/2$ prior, increase by nearly 50%. Nevertheless, BEAMS does remarkably well at determining the Gaussian distributions of SNe Ia and CCSNe with relatively little information. This is helped by the fact that because SNe Ia have a factor of ~ 20 lower dispersion than CCSNe, a loose prior on BEAMS free parameters is sufficient to find the most probable Gaussian distributions.

If we use a more flexible CC SN model (a two Gaussian or skewed Gaussian CC SN model), the requirements on our prior probabilities must become more stringent to yield precise distances. First, prior probabilities can no longer be re-normalized or shifted (Eq. 7) – these are parameters which can greatly improve the results for alternative prior probability methods. Second, our prior probabilities must be significantly more accurate to yield results with low uncertainties. With the two-Gaussian CC SN model, the uncertainty on w increases by 20% when using GalSNID priors and 100% when setting $P(\text{Ia}) = 1/2$ for all photometric SNe. Using the skewed Gaussian model, GalSNID and $P(\text{Ia}) = 1/2$ priors increase the uncertainties by 13% and 27%, respectively. Note that GalSNID classifications yield more precise measurements than a simple $P(\text{Ia}) = 1/2$ prior in these cases.

Fortunately, a single Gaussian model for CCSNe appears to yield unbiased distances even though the simulated distribution is not perfectly Gaussian. In essence, BEAMS attempts only to determine the Gaussian distributions of two types of SNe and fortunately, those distributions are relatively well-separated in dispersion even if they are not always well-separated in distance.

9. CONCLUSIONS

We measured spectroscopic redshifts for 3,073 SN host galaxies in Pan-STARRS, nearly 1,000 of which are cosmologically-useful, likely SNe Ia. When combined with the full PS1 spectroscopic sample (Scolnic et al. in prep.), we will have at least 1,092 cosmologically-useful SNe Ia from PS1.

We find that currently available CC SN templates and luminosity functions are biased and incomplete. Our results suggest there are too few bright CCSNe in our simulations.

We generate 25 simulations that closely resemble our sample. Each has 1,000 photometric PS1 SNe and 250 low- z spectroscopically-confirmed SNe Ia. These simulations show that our method can measure w with a bias due to CC SN contamination of just -0.0034 ± 0.0020 , 7% of the statistical uncertainty on w . This equates to a systematic uncertainty on w of just 0.005, but this uncertainty could be affected by incomplete knowledge of the CC SN distribution. The SN Ia dispersion, σ_{Ia} , is biased by -0.005 ($\sim 0.5\sigma$), the SALT2 shape parameter α is

biased by ~ 0.005 ($\sim 1\sigma$), and the color parameter β is biased by ~ 0.1 ($\sim 1.5\sigma$). The statistical uncertainties on w are nearly equivalent to those using only SNe Ia.

Using several variants of the method, we conservatively estimate the systematic error introduced by CC SN contamination to be 0.018 ± 0.009 (39% of the statistical error). This systematic error can be reduced to 30% by fixing α and β to the values from a spectroscopic sample or using a cut on prior probabilities from one variant to reduce CCSNe in the sample for the other variants. If α and β are fixed to known values from a spectroscopic sample, our *least* accurate classifiers, *Fitprob* and GalSNID, are able to measure w with mean bias of just 0.006.

Included in these variants are a total of four different classification methods to measure cosmology, including a host galaxy spectrum-based version of GalSNID (Foley & Mandel 2013) that we introduce in this work (see Appendix). GalSNID is based only on SN Ia host galaxy observables and a rates prior. GalSNID provides a new method of measuring w from photometric data that does not depend on SN light curves and training on simulated data. Machine learning techniques may be able to improve on the efficiency of this method in the future.

By drawing random samples from real PS1 data, we tested whether the BEAMS method can work on real data within the confidence intervals of Rest et al. (2014). We found that our measurements of w were fully consistent with Rest et al. (2014), as were the SN nuisance parameters α and β .

Though our results are robust, w is an extremely sensitive measurement and the burden of proof for BEAMS is high. Future validation tests could include SDSS and SNLS photometric data, as well as simulated tests with a variety of CC SN LFs. Additional light curve classification methods could also help to improve the reliability of the BEAMS method.

Future SN Ia samples from DES and LSST will be unable to rely solely on spectroscopic classification to measure cosmological parameters. With the light curve classification and Bayesian methodologies presented here, we validate some of the techniques that will be used in future surveys, and anticipate that PS1 photometric SNe can provide a robust measurement of w using the largest SN Ia sample to date.

This manuscript is based upon work supported by the National Aeronautics and Space Administration under Contract No. NNG16PJ34C issued through the *WFIRST* Science Investigation Teams Programme. R.J.F. and D.S. were supported in part by NASA grant 14-WPS14-0048. The UCSC group is supported in part by NSF grant AST-1518052 and from fellowships from the Alfred P. Sloan Foundation and the David and Lucile Packard Foundation to R.J.F. This work was supported in part by the Kavli Institute for Cosmological Physics at the University of Chicago through grant NSF PHY-1125897 and an endowment from the Kavli Foundation and its founder Fred Kavli. D.S. gratefully acknowledges support from NASA grant 14-WPS14-0048. D.S. is supported by NASA through Hubble Fellowship grant HST-HF2-51383.001 awarded by the Space Telescope Science Institute, which is operated by the Association of Univer-

sities for Research in Astronomy, Inc., for NASA, under contract NAS 5-26555.

Many of the observations reported here were obtained at the MMT Observatory, a joint facility of the Smithsonian Institution and the University of Arizona. This paper uses data products produced by the OIR Telescope Data Center, supported by the Smithsonian Astrophysical Observatory. Additional data are thanks to the Anglo Australian Telescope, operated by the Australian Astronomical Observatory, through the National Optical Astronomy Observatory (NOAO PropID: 2014B-N0336; PI: D. Jones). We also use data from observations at Kitt Peak National Observatory, National Optical Astronomy Observatory, which is operated by the Association of Universities for Research in Astronomy (AURA) under a cooperative agreement with the National Science Foundation. Also based on observations obtained with the Apache Point Observatory 3.5-meter telescope, which is owned and operated by the Astrophysical Research Consortium.

The computations in this paper used a combination of three computing clusters. BEAMS analysis was performed using the University of Chicago Research Computing Center and the Odyssey cluster at Harvard University. We are grateful for the support of the University of Chicago Research Computing Center for assistance with the calculations carried out in this work. The Odyssey cluster is supported by the FAS Division of Science, Research Computing Group at Harvard University. Supernova light curve reprocessing would not have been possible without the Data-Scope project at the Institute for Data Intensive Engineering and Science at Johns Hopkins University.

Funding for the Sloan Digital Sky Survey IV has been provided by the Alfred P. Sloan Foundation, the U.S. Department of Energy Office of Science, and the Participating Institutions. SDSS-IV acknowledges support and resources from the Center for High-Performance Computing at the University of Utah. The SDSS web site is www.sdss.org.

SDSS-IV is managed by the Astrophysical Research Consortium for the Participating Institutions of the SDSS Collaboration including the Brazilian Participation Group, the Carnegie Institution for Science, Carnegie Mellon University, the Chilean Participation Group, the French Participation Group, Harvard-Smithsonian Center for Astrophysics, Instituto de Astrofísica de Canarias, The Johns Hopkins University, Kavli Institute for the Physics and Mathematics of the Universe (IPMU) / University of Tokyo, Lawrence Berkeley National Laboratory, Leibniz Institut für Astrophysik Potsdam (AIP), Max-Planck-Institut für Astronomie (MPIA Heidelberg), Max-Planck-Institut für Astrophysik (MPA Garching), Max-Planck-Institut für Extraterrestrische Physik (MPE), National Astronomical Observatory of China, New Mexico State University, New York University, University of Notre Dame, Observatorio Nacional / MCTI, The Ohio State University, Pennsylvania State University, Shanghai Astronomical Observatory, United Kingdom Participation Group, Universidad Nacional Autónoma de México, University of Arizona, University of Colorado Boulder, University of Oxford, University of Portsmouth, University of Utah, University of Virginia, University of Washington, University

of Wisconsin, Vanderbilt University, and Yale University.

This research makes use of the VIPERS-MLS database, operated at CeSAM/LAM, Marseille, France. This work is based in part on observations obtained with WIRCam, a joint project of CFHT, Taiwan, Korea, Canada and France. The CFHT is operated by the National Research Council (NRC) of Canada, the Institut National des Sciences de l'Univers of the Centre National de la Recherche Scientifique (CNRS) of France, and the University of Hawaii. This work is based in part on observations made with the Galaxy Evolution Explorer (GALEX). GALEX is a NASA Small Explorer, whose mission was developed in cooperation with the Centre National d'Etudes Spatiales (CNES) of France and the Korean Ministry of Science and Technology. GALEX is operated for NASA by the California Institute of Technology under NASA contract NAS5-98034. This work is based in part on data products produced at TERAPIX available at the Canadian Astronomy Data Centre as part of the Canada-France-Hawaii Telescope Legacy Survey, a collaborative project of NRC and CNRS. The TERAPIX team has performed the reduction of all the WIRCAM images and the preparation of the catalogues matched with the T0007 CFHTLS data release.

Funding for the DEEP2 Galaxy Redshift Survey has been provided by NSF grants AST-95-09298, AST-0071048, AST-0507428, and AST-0507483 as well as NASA LTSA grant NNG04GC89G. This research uses data from the VIMOS VLT Deep Survey, obtained from the VVDS database operated by Cesam, Laboratoire d'Astrophysique de Marseille, France. zCosmos data are based on observations made with ESO Telescopes at the La Silla or Paranal Observatories under programme ID 175.A-0839.

APPENDIX

INCORPORATING HOST SPECTRAL INFORMATION IN GALSNID

We trained GalSNID on spectral information using LOSS host galaxy spectra and spectroscopically confirmed PS1 SNe for which we have host galaxy redshifts. Relative to the PS1 spectroscopic sample, LOSS has a greater number of total SNe, and a greater diversity and number of CCSNe on which to train the data.

Spectra for $\sim 1/3$ of the LOSS sample are available from SDSS/BOSS (Alam et al. 2015; 297 spectra), and we found an additional $\sim 1/3$ (305 spectra) by querying the NASA/IPAC Extragalactic Database. In total, 67% of the 905 SNe discovered by LOSS have host galaxy spectra. In general, the SNR of these data are high (much higher on average than our redshift survey data).

PS1 spectroscopically classified 520 SNe of which ~ 150 are CCSNe and the rest are SNe Ia. Of the CCSNe, ~ 30 are SNe IIn (Drout et al. in prep), 76 are II-P or II-L (Sanders et al. 2015) and ~ 20 -30 are SNe Ib or Ic. We obtained host galaxy spectra for 354 of these SNe.

We searched for a number of prominent, observational galaxy diagnostics that correlate with the age of the host, and found that the equivalent widths of bright emission lines such as OII, OIII, H α and H β are measurable in many of our spectra. We required continuum SNR > 5 near a given line measurement for an observable to

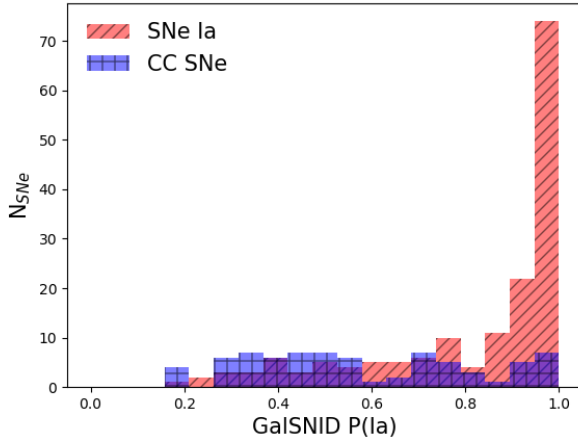


Figure 20. GalSNID classifications of spectroscopically classified CCSNe and SNe Ia in Pan-STARRS, neglecting rates priors.

be used in training or classification. As a way to incorporate additional information in a single diagnostic, we included the best matched spectral template based on cross-correlation as an observable.

Although these diagnostics are correlated, in this work we follow Foley & Mandel (2013) in treating them as independent. Final probabilities for a given SN can therefore be computed by multiplying the probability of a Ia given each observable (Foley & Mandel 2013):

$$P(\text{Ia}|D) = k^{-1} P(\text{Ia}|z) \prod_{i=1}^N P(D_i|\text{Ia}), \quad (\text{A1})$$

where N is the number of observables and $P(D_i|\text{Ia})$ is the probability of an observable given that the SN is Type Ia (Table 5). $P(D_i|\text{Ia})$ is easy to compute; it is the fraction of SNIa host galaxies that have observable D_i . $P(\text{Ia}|z)$ is a rates prior informed by our SNANA simulations. k is a normalization factor that requires $P(\text{Ia}|D) + P(\text{CC}|D) = 1$. See Foley & Mandel (2013) for additional details on the methodology. In the future, machine learning techniques may be able to improve our results by relaxing the requirement that observables be uncorrelated.

The probabilities from our LOSS+PS1 training sample are provided in Table 5. We also include effective offset, $B - K$ colors, and K absolute magnitudes using probabilities measured from Foley & Mandel (2013) and SED fits using PS1 host galaxy photometry. Note that because $H\alpha$ and $H\beta$ are almost perfectly correlated (the correlation coefficient is 0.94), we used only $H\alpha$ as an observable when it was present in optical spectra ($z \lesssim 0.35$) and $H\beta$ when it was not. Figure 13 shows the GalSNID probabilities of SNe Ia and CC SNe in PS1 and our simulations (we redshift and add noise to LOSS spectra to determine simulated GalSNID probabilities). Figure 20 shows GalSNID probabilities for real spectroscopically classified PS1 SNe.

REFERENCES

Alam, S., Albareti, F. D., Allende Prieto, C., et al. 2015, *ApJS*, 219, 12
 Arcavi, I., Gal-Yam, A., Yaron, O., et al. 2011, *ApJL*, 742, L18

Table 5
 Probability of Host Properties Given Type

Bin	$P(D_i \text{Ia})$	$P(D_i \text{Ibc})$	$P(D_i \text{II})$
Cross-Correlation Template			
absorption	0.502 ^{+0.047} _{-0.048}	0.256 ^{+0.061} _{-0.061}	0.286 ^{+0.034} _{-0.034}
ellipt+A stars	0.431 ^{+0.043} _{-0.043}	0.598 ^{+0.086} _{-0.085}	0.609 ^{+0.049} _{-0.049}
late-type	0.029 ^{+0.010} _{-0.009}	0.037 ^{+0.025} _{-0.024}	0.030 ^{+0.011} _{-0.011}
emission	0.029 ^{+0.010} _{-0.009}	0.098 ^{+0.037} _{-0.036}	0.071 ^{+0.015} _{-0.015}
$H\alpha$ Equivalent Width			
<-5.0	0.040 ^{+0.009} _{-0.009}	0.000 ^{+0.000} _{-0.000}	0.006 ^{+0.003} _{-0.003}
-5.0 – 0.0	0.217 ^{+0.022} _{-0.022}	0.072 ^{+0.031} _{-0.031}	0.088 ^{+0.017} _{-0.017}
0.0 – 5.0	0.159 ^{+0.017} _{-0.018}	0.237 ^{+0.051} _{-0.052}	0.202 ^{+0.023} _{-0.022}
5.0 – 10.0	0.097 ^{+0.015} _{-0.016}	0.124 ^{+0.031} _{-0.031}	0.153 ^{+0.019} _{-0.020}
>10.0	0.356 ^{+0.029} _{-0.029}	0.557 ^{+0.072} _{-0.072}	0.528 ^{+0.039} _{-0.040}
$H\beta$ Equivalent Width			
<-5.0	0.078 ^{+0.014} _{-0.013}	0.010 ^{+0.010} _{-0.011}	0.009 ^{+0.006} _{-0.005}
-5.0 – 0.0	0.419 ^{+0.031} _{-0.031}	0.299 ^{+0.052} _{-0.052}	0.310 ^{+0.029} _{-0.028}
0.0 – 5.0	0.341 ^{+0.026} _{-0.027}	0.423 ^{+0.062} _{-0.062}	0.432 ^{+0.034} _{-0.034}
5.0 – 10.0	0.078 ^{+0.014} _{-0.013}	0.113 ^{+0.031} _{-0.031}	0.139 ^{+0.020} _{-0.020}
>10.0	0.084 ^{+0.013} _{-0.014}	0.155 ^{+0.042} _{-0.041}	0.108 ^{+0.017} _{-0.017}
OIII Equivalent Width			
<-5.0	0.073 ^{+0.013} _{-0.013}	0.031 ^{+0.021} _{-0.021}	0.014 ^{+0.005} _{-0.006}
-5.0 – 0.0	0.195 ^{+0.020} _{-0.020}	0.155 ^{+0.042} _{-0.041}	0.102 ^{+0.017} _{-0.017}
0.0 – 5.0	0.525 ^{+0.033} _{-0.034}	0.608 ^{+0.082} _{-0.083}	0.631 ^{+0.043} _{-0.042}
5.0 – 10.0	0.086 ^{+0.013} _{-0.014}	0.093 ^{+0.031} _{-0.031}	0.082 ^{+0.014} _{-0.015}
>10.0	0.115 ^{+0.015} _{-0.016}	0.113 ^{+0.031} _{-0.031}	0.168 ^{+0.023} _{-0.022}
OII Equivalent Width			
<-5.0	0.162 ^{+0.023} _{-0.022}	0.107 ^{+0.036} _{-0.036}	0.143 ^{+0.027} _{-0.027}
-5.0 – 0.0	0.103 ^{+0.017} _{-0.017}	0.036 ^{+0.018} _{-0.018}	0.062 ^{+0.017} _{-0.018}
0.0 – 5.0	0.290 ^{+0.028} _{-0.028}	0.125 ^{+0.054} _{-0.054}	0.179 ^{+0.027} _{-0.026}
5.0 – 10.0	0.114 ^{+0.017} _{-0.017}	0.125 ^{+0.054} _{-0.054}	0.062 ^{+0.017} _{-0.018}
>10.0	0.242 ^{+0.025} _{-0.025}	0.250 ^{+0.071} _{-0.071}	0.272 ^{+0.035} _{-0.036}

Barbon, R., Benetti, S., Cappellaro, E., et al. 1995, *A&AS*, 110, 513
 Bernstein, J. P., Kessler, R., Kuhlmann, S., et al. 2012, *ApJ*, 753, 152
 Bertin, E., & Arnouts, S. 1996, *A&AS*, 117, 393
 Betoule, M., Kessler, R., Guy, J., et al. 2014, *A&A*, 568, A22
 Bianco, F. B., Modjaz, M., Hicken, M., et al. 2014, *ApJS*, 213, 19
 Blake, C., Brough, S., Couch, W., et al. 2008, *Astronomy and Geophysics*, 49, 5.19
 Blondin, S., Matheson, T., Kirshner, R. P., et al. 2012, *AJ*, 143, 126
 Brown, P. J., Breeveld, A. A., Holland, S., Kuin, P., & Pritchard, T. 2014, *Ap&SS*, 354, 89
 Campbell, H., D’Andrea, C. B., Nichol, R. C., et al. 2013, *ApJ*, 763, 88
 Childress, M., Aldering, G., Antilogus, P., et al. 2013, *ApJ*, 770, 108
 Colless, M., Peterson, B. A., Jackson, C., et al. 2003, *ArXiv Astrophysics e-prints*
 Conley, A., Guy, J., Sullivan, M., et al. 2011, *ApJS*, 192, 1
 Contreras, C., Hamuy, M., Phillips, M. M., et al. 2010, *AJ*, 139, 519
 Ergon, M., Sollerman, J., Fraser, M., et al. 2014, *A&A*, 562, A17
 Ergon, M., Jerkstrand, A., Sollerman, J., et al. 2015, *A&A*, 580, A142

- Fabricant, D., Fata, R., Roll, J., et al. 2005, *PASP*, 117, 1411
- Falck, B. L., Riess, A. G., & Hlozek, R. 2010, *ApJ*, 723, 398
- Folatelli, G., Morrell, N., Phillips, M. M., et al. 2013, *ApJ*, 773, 53
- Foley, R. J., & Mandel, K. 2013, *ApJ*, 778, 167
- Foley, R. J., Challis, P. J., Chornock, R., et al. 2013, *ApJ*, 767, 57
- Foreman-Mackey, D., Hogg, D. W., Lang, D., & Goodman, J. 2013, *PASP*, 125, 306
- Frieman, J. A., Bassett, B., Becker, A., et al. 2008, *AJ*, 135, 338
- Ganeshalingam, M., Li, W., Filippenko, A. V., et al. 2010, *ApJS*, 190, 418
- Garilli, B., Guzzo, L., Scodeggio, M., et al. 2014, *A&A*, 562, A23
- Garnavich, P. M., Bonanos, A. Z., Krisciunas, K., et al. 2004, *ApJ*, 613, 1120
- Guillochon, J., Parrent, J., & Margutti, R. 2016, *ArXiv e-prints*
- Gupta, R. R., Kuhlmann, S., Kovacs, E., et al. 2016, *ArXiv e-prints*
- Guy, J., Astier, P., Baumont, S., et al. 2007, *A&A*, 466, 11
- Guy, J., Sullivan, M., Conley, A., et al. 2010, *A&A*, 523, A7
- Hamuy, M., Folatelli, G., Morrell, N. I., et al. 2006, *PASP*, 118, 2
- Hlozek, R., Kunz, M., Bassett, B., et al. 2012, *ApJ*, 752, 79
- Hsiao, E. Y., Conley, A., Howell, D. A., et al. 2007, *ApJ*, 663, 1187
- Jerkstrand, A., Ergon, M., Smartt, S. J., et al. 2015, *A&A*, 573, A12
- Jha, S., Kirshner, R. P., Challis, P., et al. 2006, *AJ*, 131, 527
- Jones, D. H., Read, M. A., Saunders, W., et al. 2009, *MNRAS*, 399, 683
- Jones, D. O., Scolnic, D. M., & Rodney, S. A. 2015, *PythonPhot: Simple DAOPHOT-type photometry in Python*, *Astrophysics Source Code Library*
- Kaiser, N., Burgett, W., Chambers, K., et al. 2010, in *Society of Photo-Optical Instrumentation Engineers (SPIE) Conference Series*, Vol. 7733, *Society of Photo-Optical Instrumentation Engineers (SPIE) Conference Series*, 0
- Kelly, B. C. 2007, *ApJ*, 665, 1489
- Kelly, P. L., Hicken, M., Burke, D. L., Mandel, K. S., & Kirshner, R. P. 2010, *ApJ*, 715, 743
- Kessler, R., & Scolnic, D. 2016, *ArXiv e-prints*
- Kessler, R., Becker, A. C., Cinabro, D., et al. 2009a, *ApJS*, 185, 32
- Kessler, R., Bernstein, J. P., Cinabro, D., et al. 2009b, *PASP*, 121, 1028
- Kessler, R., Bassett, B., Belov, P., et al. 2010, *PASP*, 122, 1415
- Kessler, R., Marriner, J., Childress, M., et al. 2015, *AJ*, 150, 172
- Kunz, M., Bassett, B. A., & Hlozek, R. A. 2007, *Phys. Rev. D*, 75, 103508
- Kurtz, M. J., & Mink, D. J. 1998, *PASP*, 110, 934
- Lampeitl, H., Smith, M., Nichol, R. C., et al. 2010, *ApJ*, 722, 566
- Le Fèvre, O., Vettolani, G., Garilli, B., et al. 2005, *A&A*, 439, 845
- Leaman, J., Li, W., Chornock, R., & Filippenko, A. V. 2011, *MNRAS*, 412, 1419
- Lewis, A., & Bridle, S. 2002, *Phys. Rev. D*, 66, 103511
- Li, W., Leaman, J., Chornock, R., et al. 2011, *MNRAS*, 412, 1441
- Lilly, S. J., Le Fèvre, O., Renzini, A., et al. 2007, *ApJS*, 172, 70
- Lochner, M., McEwen, J. D., Peiris, H. V., Lahav, O., & Winter, M. K. 2016, *ArXiv e-prints*
- Lunnan, R., Chornock, R., Berger, E., et al. 2015, *ApJ*, 804, 90
- Matheson, T., Kirshner, R. P., Challis, P., et al. 2008, *AJ*, 135, 1598
- Metlova, N. V., Tsvetkov, D. Y., Shugarov, S. Y., Esipov, V. F., & Pavlyuk, N. N. 1995, *Astronomy Letters*, 21, 598
- Mink, D. J., Wyatt, W. F., Caldwell, N., et al. 2007, in *Astronomical Society of the Pacific Conference Series*, Vol. 376, *Astronomical Data Analysis Software and Systems XVI*, ed. R. A. Shaw, F. Hill, & D. J. Bell, 249
- Modjaz, M., Li, W., Filippenko, A. V., et al. 2001, *PASP*, 113, 308
- Modjaz, M., Blondin, S., Kirshner, R. P., et al. 2014, *AJ*, 147, 99
- Möller, A., Ruhlmann-Kleider, V., Leloup, C., et al. 2016, *ArXiv e-prints*
- Newman, J. A., Cooper, M. C., Davis, M., et al. 2013, *ApJS*, 208, 5
- Nugent, P., Kim, A., & Perlmutter, S. 2002, *PASP*, 114, 803
- Padmanabhan, N., Schlegel, D. J., Finkbeiner, D. P., et al. 2008, *ApJ*, 674, 1217
- Pastorello, A., Kasliwal, M. M., Crockett, R. M., et al. 2008, *MNRAS*, 389, 955
- Perlmutter, S., Aldering, G., Goldhaber, G., et al. 1999, *ApJ*, 517, 565
- Press, W. H. 1997, in *Unsolved Problems in Astrophysics*, ed. J. N. Bahcall & J. P. Ostriker, 49–60
- Rest, A., Stubbs, C., Becker, A. C., et al. 2005, *ApJ*, 634, 1103
- Rest, A., Scolnic, D., Foley, R. J., et al. 2014, *ApJ*, 795, 44
- Richardson, D., Jenkins, III, R. L., Wright, J., & Maddox, L. 2014, *AJ*, 147, 118
- Richardson, D., Thomas, R. C., Casebeer, D., et al. 2001, in *Bulletin of the American Astronomical Society*, Vol. 33, *American Astronomical Society Meeting Abstracts*, 1428
- Richmond, M. W., Treffers, R. R., Filippenko, A. V., & Paik, Y. 1996, *AJ*, 112, 732
- Riess, A. G., Filippenko, A. V., Challis, P., et al. 1998, *AJ*, 116, 1009
- Rodney, S. A., Riess, A. G., Strolger, L.-G., et al. 2014, *AJ*, 148, 13
- Rubin, D., Aldering, G., Barbary, K., et al. 2015, *ApJ*, 813, 137
- Sako, M., Bassett, B., Connolly, B., et al. 2011, *ApJ*, 738, 162
- Sako, M., Bassett, B., Becker, A. C., et al. 2014, *ArXiv e-prints*
- Sanders, N. E., Soderberg, A. M., Gezari, S., et al. 2015, *ApJ*, 799, 208
- Schlafly, E. F., Finkbeiner, D. P., Jurić, M., et al. 2012, *ApJ*, 756, 158
- Scolnic, D., & Kessler, R. 2016, *ArXiv e-prints*
- Scolnic, D., Rest, A., Riess, A., et al. 2014a, *ApJ*, 795, 45
- Scolnic, D., Casertano, S., Riess, A., et al. 2015, *ApJ*, 815, 117
- Scolnic, D. M., Riess, A. G., Foley, R. J., et al. 2014b, *ApJ*, 780, 37
- Shivvers, I., Mazzali, P., Silverman, J. M., et al. 2013, *MNRAS*, 436, 3614
- Shivvers, I., Modjaz, M., Zheng, W., et al. 2016, *ArXiv e-prints*
- Silverman, J. M., Foley, R. J., Filippenko, A. V., et al. 2012, *MNRAS*, 425, 1789
- Smee, S. A., Gunn, J. E., Uomoto, A., et al. 2013, *AJ*, 146, 32
- Smith, M., Bacon, D. J., Nichol, R. C., et al. 2014, *ApJ*, 780, 24
- Stetson, P. B. 1987, *PASP*, 99, 191
- Stritzinger, M. D., Phillips, M. M., Boldt, L. N., et al. 2011, *AJ*, 142, 156
- Suh, H., Yoon, S.-c., Jeong, H., & Yi, S. K. 2011, *ApJ*, 730, 110
- Sullivan, M., Le Borgne, D., Pritchett, C. J., et al. 2006, *ApJ*, 648, 868
- Sullivan, M., Guy, J., Conley, A., et al. 2011, *ApJ*, 737, 102
- Taubenberger, S., Hachinger, S., Pignata, G., et al. 2008, *MNRAS*, 385, 75
- Taubenberger, S., Navasardyan, H., Maurer, J. I., et al. 2011, *MNRAS*, 413, 2140
- Tonry, J., & Davis, M. 1979, *AJ*, 84, 1511
- Tonry, J. L., Stubbs, C. W., Lykke, K. R., et al. 2012, *ApJ*, 750, 99
- Toth, I., & Szabó, R. 2000, *A&A*, 361, 63
- Tripp, R. 1998, *A&A*, 331, 815
- Tsvetkov, D. Y., Volkov, I. M., Baklanov, P., Blinnikov, S., & Tsuchin, O. 2009, *Peremennye Zvezdy*, 29
- Yaron, O., & Gal-Yam, A. 2012, *PASP*, 124, 668